NASA-TM-83497

DOE/NASA/51044-34
NASA TM-83497

NASA-TM-83497
19840011948

Road Load Simulator Tests of the Gould Phase I Functional Model Silicon Controlled Rectifier ac Motor Controller for Electric Vehicles

Francis Gourash
National Aeronautics and Space Administration
Lewis Research Center

February 1984

Prepared for
U.S. DEPARTMENT OF ENERGY
Conservation and Renewable Energy
Office of Vehicle and Engine R&D

Printed in the United States of America

Available from
National Technical Information Service
U.S. Department of Commerce
5285 Port Royal Road
Springfield, VA 22161

NTIS price codes[1]
Printed copy: A04
Microfiche copy: A01

---

[1] Codes are used for pricing all publications. The code is determined by the number of pages in the publication. Information pertaining to the pricing codes can be found in the current issues of the following publications, which are generally available in most libraries: *Energy Research Abstracts (ERA); Government Reports Announcements* and Index (*GRA* and I); *Scientific and Technical Abstract Reports (STAR);* and publication, NTIS-PR-360 available from NTIS at the above address.

```
 50       1       1 RN/NASA-TM-83497
              DISPLAY 50/2/1
       84N20016*#   ISSUE 10   PAGE 1529   CATEGORY 44   RPT#: NASA-TM-83497
       E-1831 NAS 1.15:83497 DOE/NASA/51044-34   CNT#: DE-AI01-77CS-51044
       84/02/00  70 PAGES   UNCLASSIFIED DOCUMENT
UTTL:  Road load simulator tests of the Gould phase 1 functional model silicon

       Final Report
AUTH:  A/GOURASH, F.
CORP:  National Aeronautics and Space Administration. Lewis Research Center,
       Cleveland, Ohio.     AVAIL.NTIS   SAP: HC A04/MF A01
MAJS:  /*ELECTRIC MOTOR VEHICLES/*SILICON CONTROLLED RECTIFIERS/*SIMULATORS
MINS:  / DYNAMIC TESTS/ EFFICIENCY/ INDUCTION MOTORS/ LOADS (FORCES)
ABA:   Author
ABS:   The test results for a functional model ac motor controller for electric
       vehicles and a three-phase induction motor which were dynamically tested
       on the Lewis Research Center road load simulator are presented. Results
       show that the controller has the capability to meet the SAE-J227a D cycle
       test schedule and to accelerate a 1576-kg (3456-lb) simulated vehicle to a
       cruise speed of 88.5 km/hr (55 mph). Combined motor controller efficiency
       is 72 percent and the power inverter efficiency alone is 89 percent for
       the cruise region of the D cycle. Steady state test results for motoring,
       regeneration, and thermal data obtained by operating the simulator as a
       conventional dynamometer are in agreement with the contractor's previously
ENTER:
```

DOE/NASA/51044-34
NASA TM-83497

Road Load Simulator Tests of the Gould Phase I Functional Model Silicon Controlled Rectifier ac Motor Controller for Electric Vehicles

Francis Gourash
National Aeronautics and Space Administration
Lewis Research Center
Cleveland, Ohio 44135

February 1984

Work performed for
U.S. DEPARTMENT OF ENERGY
Conservation and Renewable Energy
Office of Vehicle and Engine R&D
Washington, D.C. 20545
Under Interagency Agreement DE-AI01-77CS51044

N84-20016#

ROAD LOAD SIMULATOR TESTS OF THE GOULD PHASE I FUNCTIONAL MODEL SILICON CONTROLLED RECTIFIER ac MOTOR CONTROLLER FOR ELECTRIC VEHICLES

Francis Gourash

National Aeronautics and Space Administration
Lewis Research Center
Cleveland, Ohio 44135

E-1831

SUMMARY

Under contract, DEN 3-60 sponsored by the Department of Energy (DOE) and managed by NASA Lewis Research Center, the phase I functional model silicon controlled rectifier (SCR) ac motor controller was developed by Gould Laboratories of Gould, Incorporated. This controller was developed to demonstrate the use of state-of-the-art power SCR semiconductors and a microprocessor-based logic and control system in an ac motor controller for electric vehicle propulsion systems. The controller and its steady state characteristics are described in the contractor's report DOE/NASA/0060-82/1, NASA-CR-167919. This report complements the contractor's report and discusses the results of dynamic and steady state tests of this controller on the Lewis road load simulator.

The dynamic tests were performed under simulated vehicle driving conditions in accordance with the Society of Automotive Engineers test procedure J227a (SAE-J227a) driving cycle schedules. Road loading was adjusted to simulate a vehicle weight of 1567 kg (3456 lb), rolling tire radius of 0.267 m (0.875 ft), and zero grade on a smooth road. Tests were run in fixed overall gear ratios of 8.22:1 and 19.68:1. Steady state tests for motoring, regenerating, and thermal data were run by operating the road load simulator as a conventional dynamometer.

Test results verify the feasibility of ac motor controllers with state-of-the-art power SCR semiconductors and microprocessor-based logic and control circuits. They also show that the functional model controller has the power capability to meet the SAE-J227a schedule D driving cycle requirements and accelerate a vehicle to a cruise speed of 88.5 km/hr (55 mph). Its regeneration capability will reduce the energy requirements of electric vehicles by returning braking energy to the battery. The combined motor controller efficiency during the cruise region of the D cycle is 72 percent; efficiency of the power inverter for this same region is 89 percent. Observed improvements in schedule B driving cycle performance in a higher overall gear ratio of 19.68:1 may be applicable to schedule D driving cycle performance by the use of a two-speed transmission. Since most electric vehicle propulsion systems to date have used dc motors and controllers, the dynamic and steady state test results provide a data base for further development of ac motor controllers and propulsion systems.

A phase II engineering model of this controller developed by Gould under contract DEN 3-249 uprates the power for diesel equivalent vehicle performance and incorporates integral onboard battery-charging capability. The inverter module package is redesigned for smaller volume, lower weight, and improved thermal management. Improved components are used in the commutation circuits.

INTRODUCTION

The road load simulator (RLS) is a unique facility at NASA Lewis Research Center that facilitates dynamic testing of components and complete propulsion systems for electric vehicles (ref. 1). It enables the application of road loads normally experienced in a vehicle to a propulsion system so that an investigation and evaluation of a component's performance and interaction with the system under dynamic driving conditions can be made. This facility was used to test the phase I functional model silicon controlled rectifier ac motor controller and its load motor. This report, therefore, is a test report that presents and discusses the effects of dynamic testing on the internal parameters of the dc power source, the controller, and load motor considered as a subsystem of the overall propulsion system. These data are significant to future continuing development of ac propulsion systems since, prior to this time, most electric vehicles used dc motors and dc controllers for their propulsion systems.

The phase I functional model SCR ac motor controller was developed by Gould Laboratories under contract DEN 3-60 sponsored by the Department of Energy (DOE). This contract was initiated by Lewis in 1979 and represents, in part, NASA's support to the DOE Electric and Hybrid Vehicle program. The purpose of this contract was to demonstrate the feasibility of and develop the technology for an ac motor controller using low-cost, state-of-the-art power SCR semiconductors with microprocessor-based logic and control circuits. The load motor for the controller is a conventional ac induction motor. The resulting functional model controller is described in the final report (DOE/NASA/0060-82/1, NASA-CR-167919, (ref. 2)). This test report presents additional data and complements the contractor's report.

Results for RLS tests in accordance with the Society of Automotive Engineers test procedure J227a (SAE-J227a) driving cycle schedules are presented and discussed. Emphasis is placed on the schedule D driving cycle and vehicle acceleration to a speed of 88.5 km/hr (55 mph) since the controller design was based on achieving these performance characteristics. Results for schedules B and C driving cycles are also included. Results of thermal tests under two different operating modes of the controller are presented, and steady state test results for motoring and regeneration operating modes of the controller and motor are presented in appendixes B, C, and D. Steady state tests were run by operating the RLS as a conventional dynamometer. Appendix A defines the B, C, and D driving cycle schedules and the road loading for the dynamic tests. Brief descriptions of controller circuits, motor, test layout and procedures, and instrumentation are included. Operational test problems experienced in the test program are described. Concluding remarks are based on results obtained. A description of the phase II follow-on engineering model of the controller is also included. The primary units in this report are of the International System of Units (SI); corresponding conventional units are given in parentheses and as separate axes for curves and graphs.

CONTROLLER MOTOR SYSTEM

System Concept

The concept for the functional model controller and motor system uses a dc-to-three-phase inverter to power a conventional three-phase squirrel cage induction motor. The motor is modified for high-speed operation in conjunction with a fixed ratio transmission for the propulsion system. The inverter produces three-phase power at variable voltage and frequency to provide the motor speed and torque demands over the motor's operating ranges. The control strategy is a standard motor slip control technique with motor voltage control for constant air gap magnetic flux (V/Hz) operation of the motor. The motor slip frequency is proportional to the torque demand from the motor, and the motor's rotor speed is fed back to logic circuits by an optical tachometer mounted on the motor shaft. The two frequencies are summed to determine the excitation frequency applied to the motor and its resulting synchronous speed. Motor voltage is controlled by pulse width modulation (PWM) of the dc source voltage in the constant torque region of operation for motor speeds from zero to the base speed of the motor. At higher motor speeds the voltage applied to the motors is a variable frequency quasi-square wave of constant amplitude determined by the battery voltage. This region of operation results in a constant horsepower mode of operation at decreasing motor air gap magnetic flux. Motor slip is positive for motoring operation and is negative for regeneration during braking operation. A negative motor slip is produced by decreasing the motor excitation frequency below the motor rotor's rotational frequency.

Inverter Power Design Considerations

The inverter power stage was designed to a power capability for a 1587-kg (3500-lb) vehicle to meet the SAE-J227a schedule D driving cycle requirements and for a cruising speed of 88.5 km/hr (55 mph). Direct current power is to be obtained from a battery pack consisting of 20 conventional lead-acid 6-V battery modules. The 20 modules are series connected for a nominal dc operating voltage of 120 V.

A fixed ratio transmission with an overall gear ratio of 9.8:1 was intended for the propulsion system using this motor and controller and was considered in the design of the power inverter. Additional vehicle parameters that were considered are a vehicle frontal area of 1.86 m^2 (20 ft^2), 0.33-m (13-in.) diameter wheels, and an aerodynamic drag coefficient of 0.30.

Component Descriptions

Brief descriptions of the inverter, control circuits, and load motor will be given since complete descriptions are presented in the final report (NASA-CR-167919).

Power inverter. - The schematic circuit diagram of the power inverter is shown in figure 1. This is a conventional three-phase bridge circuit consisting of power SCR semiconductors SCR1 to SCR6 and power reactive diodes D1 to D6. The reactive diodes provide current paths for continuity in the flow of reactive motor currents and also for the transfer of braking energy to the battery during regeneration operation of the motor and vehicle braking. The inverter circuit uses bus commutation to commutate the bridge SCRs. The positive bus SCRs (SCR1, SCR3, SCR5) are commutated off together by gating and firing SCR7, and the negative bus SCRs (SCR2, SCR4, SCR6) are commutated by SCR8. Excess commutation energy is recovered and returned to the battery through auxiliary windings T1C and T2C on the commutation transformers and SCR9 and SCR10.

The inverter provides the three-phase power at variable voltage and frequency to operate the motor over its speed and torque ranges. The inverter produces a PWM motor voltage for constant V/Hz and constant torque operation of the motor, and a quasi-square wave motor voltage at high motor speeds for constant horsepower motor operation.

Control circuits. - The inverter operation and switching are directed by a control strategy that uses both slip frequency and motor air gap magnetic flux control. Two control loop circuits, a frequency loop and a voltage loop, under the supervision of a Motorola 6802 microprocessor and appropriate algorithms, implement this strategy. In the frequency loop, the slip frequency is added to the rotor rotational frequency which is fed back by the optical tachometer. The sum of these two frequency signals determines the excitation frequency applied to the motor. The summation is made in a phase-lock-loop circuit. The phase-lock-loop technique is used for accuracy and stability considerations because the summation involves a low slip frequency and a much higher rotor frequency.

The voltage loop produces the PWM gating signals required for constant air gap magnetic flux operation of the motor and also those for motor operation with quasi-square wave voltages. The sine-triangle technique is used to generate the PWM signals. In its basic form this technique compares a sine wave signal with a triangular wave form signal at the input of a voltage level detector. The output from the detector changes its state when the magnitudes of the two input signals are equal, that is, intersect each other. The technique is illustrated in figure 2 for triangle/sine frequency ratios of 9:1 and 27:1. The resulting output from the detector is the square wave pulse train shown as motor voltage. The fundamental frequency of the motor voltage waveform is the frequency of the sine wave for both ratios shown.

The Gould controller uses high pulsing rates of PWM at low motor speed to minimize harmonic motor currents and pulsating torques. The pulse rate is changed by changing the frequency of the triangular waveform signal as illustrated in figure 2 for the two triangle/sine frequency ratios. In this controller the pulse rate is changed in discrete triangle/sine ratios of 81:1, 63:1, 45:1, and 27:1 over a motor speed range from 0 to 86.4 rad/sec (825 rpm). For higher motor speeds extending to the transition from PWM to quasi-square wave operation the triangle/sine ratio is fixed at 9:1. Photographs of sine, triangle, and PWM waveforms from the functional model voltage loop circuit for three motor speeds are shown in figure 3.

The magnitudes of the sine and triangle signals are determined by algorithms in the microprocessor circuit. For quasi-square wave motor voltage operation the magnitudes are increased to saturate the level detector. The voltage waveform then is a quasi-square wave of constant amplitude but of variable frequency determined by the frequency of the reference sine wave. Photographs of this waveform are shown in figure 57 of appendix B at motor speeds of 4316 and 4995 rpm. Notches in the waveform result from bus commutation of the inverter SCRs. The series of photographs of motor voltage and current in this figure illustrate that the transition from PWM to quasi-square wave operation is not an abrupt transition but takes place over a wide range of motor speed.

In addition to the loop control functions described, the microprocessor also performs the tasks of logic sequencing, thermal protection of power components, and interlocking against damaging commands.

Motor. - The motor selected as a motor load for the functional model controller is a standard line Gould E+ motor. It is a three-phase, four-pole, cast aluminum squirrel cage induction motor. The National Electrical Manufacturers Association (NEMA) frame designation is 215 totally enclosed and non-ventilated (TENV). The nominal horsepower rating is 10 hp at 230 V and 60 Hz. The motor was modified to operate over a speed range of 0 to 838 rad/sec (8000 rpm). Modifications consisted of replacing the bearings with class C clearance bearings, removing the rotor cooling fins, balancing the rotor for high speed, and rewinding the motor for 36 V at 60 Hz.

Fabricated components. - The components fabricated for the functional model controller and motor system are shown in the photograph in figure 4. This photograph shows the motor, inverter, and control module. The small box atop the control module contains a switch to simulate the forward-neutral-reverse directional selector of a vehicle and potentiometers to simulate the accelerator and brake pedals. Figure 5 is a photograph of the inverter and control modules with their covers removed.

Test Layout, Instrumentation, and Procedures

Layout. - A sketch of the general test layout is shown in figure 6. An available transaxle with suitable gear ratios was used for motor speed reduction for compatibility with the RLS input speed requirements. The transaxle from the Eaton Corporation ac propulsion system (refs. 3 and 4) was used for this purpose. The motor and transaxle are coupled to the RLS through the input gearbox as shown. Road load is provided by the hydroviscous absorber, and vehicle inertia is simulated by the inertia wheels of the RLS. Transducers measure motor output torque and speed and transaxle output torque and speed applied to the RLS. The motor and controller inverter module are cooled by forced air blowers. The cooling fixture for the inverter is wedge-shaped to direct the air flow over the rear-mounted commutation transformers. A vent was fabricated in the inverter module front cover to exhaust the internal fan circulated air flow.

Direct current power was obtained from either the 120-V battery pack or the battery simulator supply by a selector switch. The simulator supply is a dc motor generator set with a large output filter capacitor bank. It provides a variable dc output voltage and circumvents the problems of state-of-charge, temperature, discharge rates, and recharging normally experienced with batteries. The instruments were mounted in an instrument rack and the test data were collected and processed by the Lewis data system. Tests were controlled from the adjoining control room which also contained local monitors and instrument readouts.

Photographs of the actual layout are shown in figures 7 and 8. Figure 7 is a photograph of the input to the RLS showing the test controller at the right. Figure 8 is a closeup view showing the motor and transaxle coupling to the RLS.

Instrumentation. - A sketch of the instrumentation is shown in figure 9. The instrument list in table I defines the test parameters measured, identifies the instruments used, and gives the respective scale ranges. The symbol column identifies the parameters as they are processed by the data system.

Motor and battery currents are sensed by coaxial current shunts, and precision wattmeters measure dc and ac motor power. The three-wattmeter method was used to measure the three-phase motor input power. The wattmeters are high-rate sampling instruments and determine the average power over the sampling interval. Currents and voltages are measured by rms reading digital instruments. Torque and speed are measured by transformer coupled torque transducers; separate data processors for these units also produce a readout of mechanical power in kilowatts. Slip frequency and motor excitation frequencies are sensed in the logic circuitry of the controller. Fibre optic devices isolate and transmit these measurements for processing and readout. Standard thermocouples are installed within the inverter power module for temperature measurements and the motor came equipped with three thermocouples installed within the motor windings. All instruments used are rated for an accuracy of 1 percent.

Data system. - Lewis's ESCORT system was used for data acquisition. This is a high-speed sampling system that records raw data on tape and has limited computational capability for local display and monitoring of selected processed data. The recorded data is transmitted to an IBM 370 computer for complete processing. It is batch processed and then stored in a data base where it can be utilized in different forms. The computer-plotted curves in this report were plotted from such a data base.

Test Procedures

Dynamic tests. - The dynamic tests were run in accordance with the SAE-J227a, schedules B, C, and D driving cycles. These schedules are shown in appendix A. The road load was set to comply with the gear ratios of the Eaton transaxle and with the same vehicle characteristics that were used to test the Eaton propulsion system. These vehicle characteristics are as follows with gear ratios of 8.22:1 and 19.68:1.

Weight, kg (lb)	1567 (3456)
Aerodynamic drag coefficient (Cd)	0.46
Frontal area (A), m^2 (ft^2)	1.82 (19.6)
Tire radius, m (in.)	0.267 (10.5)
Tire rolling resistance per unit of vehicle weight, kg/kg (lb/lb)	0.0095 (0.0095)

The road load for these conditions and vehicle speeds up to 88.5 km/hr (55 mph) are shown in figures 53 to 55 in appendix A. This loading was held constant for all driving cycle testing.

Since vehicle braking is a total vehicle system consideration and was not addressed in this first functional model controller, it was necessary to experimentally adjust the braking provided by the RLS to run the cycle tests. This was done by running each driving cycle with an overall gear ratio of 8.22:1 and adjusting the braking effort of the RLS to the braking interval requirements of the cycles. Under these conditions the RLS is providing approximately 80 percent of the required braking effort.

The dynamic tests were run in each of the two-gear ratios with power from the battery simulator supply and the 120-V battery pack. Data were recorded in a continuous scanning mode for each test. An 8-channel Brush recorder monitored critical parameters of each test.

Steady state tests. - Steady state tests were run by operating the RLS as a conventional dynamometer in both constant speed and constant torque operating modes. Direct current power was obtained from the 120-V battery pack and the battery simulator supply. Tests were run in each of the two-gear ratios for both motoring and regeneration operating modes of the motor. The regeneration tests were run with the battery initially predischarged to a 40-percent state-of-charge level. Each test point was recorded by 10 scans of the data system. The 8-channel Brush recorder monitored each test.

TEST RESULTS AND DISCUSSION

The overall test results address the schedules B, C, and D driving cylces, the effects of power supply characteristics and source voltage variations, vehicle acceleration to 88.5 km/hr (55 mph), a comparison of performance in the two overall gear ratios, and thermal performance of the controller and motor. The results will be presented in accordance with the driving cycles that were used for the separate tests, and the discussions will address separate regions of the cylces (i.e., acceleration, cruise, and braking). Efficiency, energy, and stability characteristics will be discussed for various regions.

Schedule D Cycle Performance

The performance of the functional model controller and load motor as determined by RLS tests to SAE-J227a schedule D driving cycle requirements is shown by the series of curves in figures 10 to 25. Tests for these data were run in the 8.22:1 overall gear ratio, and the dc power was obtained from the battery simulator supply.

Propulsion system speed response. - The propulsion system's speed response to a command for the schedule D cycle is shown in figure 10. The system includes the controller, load motor, and the transaxle. The curve is a two-axis recording of measured transaxle output shaft speed as a function of time. The axis is presented as vehicle speed in mph and is determined from the measured speed and rolling radius of the tires. The adjacent Y-axis scale of motor speed in rpm is included for reference, and the actual measured motor speed for this same cycle is shown in the computer-plotted curve in figure 11.

With the exception of the acceleration region, the response curve in figure 10 follows the commanded response very closely in the cruise, coast, and brake regions of the D cycle. The acceleration region and the oscillation shown at the completion of the brake region will be discussed in subsequent sections of the D cycle performance. The zero offset of the response curve in figure 10 is due in part to clutch slippage in the transaxle since vehicle speed is measured at the transaxle output shaft. Additional zero offset delays result from logic sequence functions in the controller and the time required to establish a breakaway torque in the motor. The zero offset for the curve in figure 11 does not include clutch slippage because the ordinate is the measured motor shaft speed. This offset, however, includes the logic sequencing and breakaway torque delays. It also includes a delay due to the graphics plot routine which contains a minimum plotting threshold level.

Acceleration region. - Neglecting zero offset, the acceleration times for the response curves in figures 10 and 11 are approximately 32 sec and deviate from the 28-sec commanded acceleration. Deviation results largely from the inflections in the middle of the response curves. These inflections are approximately 3 to 4 sec in width (corresponding to the deviation) and are traceable to the dips in motor torque, current, and shaft power characteristics shown in figures 12, 13, and 16, respectively. The current limiting of the battery current at a level of 330 A (fig. 14) is also contributing to the acceleration time by limiting the motor shaft power to 38.5 hp during the latter stages of the acceleration region. The calculated horsepower requirement for constant acceleration of 0.72 m/sec^2 (2.36 ft/sec^2) to the cruise speed is 39.5 hp. The curves of battery current and battery power (figs. 14 and 15) follow the motor curves during the acceleration region. The motor frequency curve for the cycle is shown in figure 18. Frequency is linearly proportional to motor speed.

Dips in the motor torque, current, and power characteristics are peculiar to not only the dynamic performance but are also evident in the steady state motoring and regenerative operating mode characteristics shown in appendixes B, C, and D. The dips occur over a motor speed range which coincides with the PWM to quasi-square wave transition region of the controller. This range extends from approximately 262 to 471 rad/sec (2500 to 4500 rpm). Typical current and voltage waveforms illustrating this transition are shown in figure 57 of appendix B.

The contractor has reported similar dips in his peak torque and power data (ref 2). His explanation is that in the transition region the voltage requests for the motor are modified by interactions of the PWM algorithm and the SCR commutation logic so that the fundamental component of motor voltage changes. The slip frequency and motor voltage curves in figures 17 and 19 tend to confirm this explanation; the slip frequency is constant at 3 Hz indicating a command for constant torque for acceleration, but the voltage curve levels off abruptly in the transition region (fig. 19).

The speed control loop for the RLS tests was closed by feedback of motor speed. The curve in figure 10, however, is for the total propulsion system response and includes transaxle and gearing characteristics. In a practical vehicle system the loop is closed by the operator and the total system response is under his control. Providing the power capability is adequate, the operator can compensate for factors impeding response (i.e., inflections, hesitations) by further depressing the accelerating pedal, thereby increasing the error signal to the controller. It will be shown in a subsequent section that this functional model controller has the power capability to meet the schedule D acceleration requirement so that the significance of the observed inflections relative to acceleration is questionable and can be compensated for by an operator.

Braking region. - The division of braking between electrical regenerative braking and mechanical brakes is a total vehicle system problem and was not addressed for the functional model controller. The braking performance shown in the cycle D performance curve (fig. 10) is due mainly to the RLS and, therefore, is not representative of the controller's regenerative braking capability. The steady state regeneration mode curves in appendix D, however, show that the functional system will provide regenerative braking down to vehicle speed of 12.9 km/hr (8 mph). The shape of a required braking characteristic with mechanical brake blending for a given vehicle is dependent to a large extent on the peak power capabilities of both motor and controller and the peak current capabilities of the power semiconductors.

Stability. - The schedule D cycle tests show a low-magnitude, low-frequency, motor shaft oscillation at the end of the braking period and essentially at zero vehicle speed (fig. 10). This oscillation is believed to be caused by a phase shift and gain adjustments in the phase-lock loop of the frequency control circuit. Circuit corrections can be made to eliminate or reduce the oscillations to a minimal tolerable level.

Cruise Region Performance

The cruise region of the schedule D driving cycle is a constant vehicle speed of 72.4 km/hr (45 mph) for a 50-sec time interval. This region corresponds to steady state operation of the motor and controller at a constant motor speed of 620 rad/sec (5921 rpm) and constant motor load torque of 11.5 Nm (102 in-lb). The characteristics to be discussed for this cruise region are motor and controller efficiency (individually and combined), energy requirements for the acceleration and cruise regions, and the effects of dc supply voltage variations.

Efficiency. - The efficiency curves for the motor and controller together as a system and individually are shown in figures 20 to 22. The efficiencies are 72 percent for the motor controller system, 81 percent for the motor, and 89 percent for the power inverter of the controller. These efficiencies are in reasonable agreement with the contractor's reported steady state results for the same speed and torque conditions.

At this cruise condition the controller is operating in the quasi-square wave mode with minimum commutations per cycle and minimum commutation losses. The motor is also operating at a more favorable operating point where losses due to harmonics and magnetic core losses are lower than for PWM operation.

Energy. - Energy required for the acceleration and cruise regions of the driving cycle was determined by integrating the instantaneous battery power over these time intervals. Integration was performed by the data processing system from battery power wattmeter readings. The energy curve in figure 23 shows the energy requirement to be 1.12 MJ (0.31 kWh). Implementation of brake blending in a vehicle application to utilize the regenerative braking capability of the controller and motor system will reduce the energy requirements per cycle by returning some of the vehicle kinetic energy to the battery.

Supply voltage variations. - The nominal battery voltage for the functional controller is 120 V dc. Schedule D cycle tests with battery simulator supply voltages of 110 and 105 V were run to determine the effects on motor speed and motor controller system efficiency. The curves in figures 24 and 25 show a 1.5-percent reduction in motor speed for the cruise region and a 2-percent reduction in motor controller efficiency for the same region. The acceleration characteristic is not significantly affected by the lower voltages. The effects observed are considered to be reasonable.

Maximum Acceleration to 88.5 km/hr (55 mph)

This test was run to determine the propulsion system's maximum acceleration to a vehicle speed of 88.5 km/hr (55 mph) and the performance of key system parameters for this condition. The transaxle was set to the 8.22:1 overall gear ratio and the battery simulator power supply was used. Test results are shown in the series of curves in figures 26 to 31.

Acceleration performance. - The motor speed response is shown in figure 26. Motor speed corresponding to 88.5 km/hr (55 mph) in this gear ratio is 759 rad/sec (7250 rpm) and the acceleration time to this speed is 44.3 sec. This gives an average acceleration of 0.55 m/sec^2 (1.24 mph/sec) for the time interval. The maximum acceleration, however, during the first quarter of the interval is 1.34 m/sec^2 (3 mph/sec). This initial acceleration is not sustained due to motor current limiting to 325 A as shown in figure 27. Current limiting in this controller is implemented in the frequency circuits by controlling slip frequency. Figure 28 shows that the slip frequency is held at 5.2 Hz to limit the motor current.

Other key parameters from figures 29 and 30 are that the maximum developed motor torque is 87.6 Nm (775 in-lb) and the maximum motor shaft power is 39.5 hp. These magnitudes approach the maximum levels of 101 Nm and 42.2 hp at a motor speed of 315 rad/sec (3008 rpm) reported by Gould but indicate there is some reserve for acceleration to an even higher vehicle speed. A top vehicle speed of 96.5 km/hr (60 mph) is a design goal for this controller.

The motor which has a nominal rating of 10 hp can develop the short term peak torque and horsepower demands (in repeated testing) with no adverse effects. The maximum battery and motor currents shown in figures 27 and 31 are on the order of 325 and 350 A, respectively. (Motor current is current limited and these are rms current values.) The power SCRs in the controller are rated for a continuous current of 250 A, rms. The SCRs also provide the short term maximum current demands with no adverse effects.

Correlation with schedule D Acceleration. - The summary statement of the section on schedule D acceleration stated that in a system with adequate power capability, impedance to a desired response could be compensated for to a limited extent by the operator. The motor speed response curve in figure 26 and the motor shaft power curve in figure 30 tend to confirm this statement. Figure 26 shows that the motor accelerates the system to the schedule D requirements (45 mph in 28 sec); a motor speed of 620 rad/sec (5920 rpm) corresponds to a vehicle speed of 72.4 km/hr (45 mph); and figure 30 shows that the peak motor power (current limited) for this acceleration is 39.5 hp. The calculated motor power required for linear acceleration of the test vehicle to the schedule D requirement is also 39.5 hp.

COMPARISON OF POWER SOURCES

The schedule D cycle was run with power from the battery and the battery simulator supplies to discern any major differences in performance due to the power supplies. Figures 32 and 33 show no major differences in motor speed response or inverter efficiency, but the acceleration time to cruise speed is slightly longer for the battery supply. The largest effect is the drop in battery terminal voltage due to its internal impedance as shown in figure 34.

The battery simulator is a stiff, low impedance supply and maintains 120 V for nearly the entire cycle. The battery supply, however, shows a 30-V droop from its no load terminal voltage in the acceleration period and a 12-V droop during the cruise part of the cycle. The battery supply's internal impedance, determined from the voltage as a function of current characteristic curve in figure 35, is 0.10 ohm. The voltage characteristic of the battery supply is reflected in the applied motor voltage as shown in figure 36, and this in turn impacts motor output power during acceleration as shown in figure 37. The reduced peak motor power with the battery supply accounts for the longer acceleration time shown in figure 32.

Comparison of Schedule B, C, and D Driving Cycles

Although the functional model controller was designed to schedule D driving cycle requirements, the propulsion system was also tested to the schedule B and C driving cycles mainly for additional performance information. The tests were run in the 8.22:1 overall gear ratio and dc power was obtained from the battery simulator supply.

The motor speed response curves for the three driving cycle schedules are shown in figure 38. Comparisons of motor torque, battery current, and motor power are shown in figures 39, 40, and 41, respectively. The efficiency curves in figure 42 show a higher efficiency for schedule C cycle operation than for the schedule B cycle. The factors contributing to a higher C cycle efficiency are a higher operating power level and controller and motor operation with nearly quasi-square wave voltage waveforms at the higher motor speed. The controller and motor operate in the PWM mode throughout the entire schedule B cycle in this gear ratio. The above efficiency curves tend to verify that the functional model controller was designed to perform to the schedule D cycle.

Effects of Gear Ratios on Schedule B Cycle Performance

The propulsion system was operated over the schedule B driving cycle with the transaxle fixed for an overall gear ratio of 19.68:1. The B cycle performance curves for an overall gear ratio of 8.22:1 are included in the following set of curves for comparative purposes.

The motor speed response curve in figure 43 shows that motor speed is 659 rad/sec (6297 rpm) in the cruise region of the cycle in this gear ratio. The larger torque multiplication of the higher gear ratio reduces peak motor torque requirements for acceleration by a factor of approximately 1.9 (fig. 44) and also reduces the corresponding peak motor current by a factor of approximately 1.7 (fig. 45). In the 19.68:1 overall gear ratio the motor current reaches the current limit of 325 A set for the controller. The advantages provided by the 19.68:1 overall gear ratio for schedule B cycle operation are that the controller passes through the higher loss PWM operating region quickly during acceleration and operates in the lower loss quasi-square wave operating mode during the cruise region of the cycle. This results in a substantial decrease in battery power (fig. 46) with a corresponding increase in motor controller efficiency (fig. 47). This result suggests that it may be desirable to use a two-speed transmission for schedule D cycle operation to increase efficiency and improve on overall performance.

Thermal Tests

Thermal tests were performed to measure power inverter module and motor temperatures for both PWM and quasi-square wave operating modes. Motor loading was kept constant at 15 hp for both tests. Motor speed was kept constant at 262 rad/sec (2500 rpm) for PWM operation and at 628 rad/sec (6000 rpm) for quasi-square wave operation. The road load simulator was operated as a conventional dynamometer for the thermal tests. Test results are shown in figures 48 and 49.

PWM operating mode. - The thermal curves in figure 48 show rapid temperature rises for the commutating capacitor, inverter module internal ambient, and the motor windings. The operating time prior to shutdown by the thermal protection circuit was 13 min. This result was expected for PWM operation because commutation losses are high and the motor current is also high at this speed for the high motor load.

Quasi-square wave operating mode. - The thermal curves in figure 49 for quasi-square wave operation show considerably lower temperatures for the commutating capacitor and inverter internal ambient. These temperatures result from lower commutation losses and lower motor current at the same load but higher motor speed.

The motor winding temperature shows a constant rate of temperature rise for the first 25 min of the test and then the rate begins to taper and decrease for the remainder of the test. The motor winding temperature stabilizes at a temperature of 110° C in 1 hr for this load and speed condition.

Operational Test Problems

The problems encountered in the test program were of the nuisance types. Two are temperature-related and another is the audio noise of the controller. One temperature problem results from the tachometer and the other from the commutation circuit components. The audio noise results from the laminated core in the commutation transformer.

Tachometer. - The tachometer is an optical device with the encoder mounted to the motor end bell and the slotted disc mounted directly on the motor shaft. The semiconductors in the encoder are rated for a temperature of only 50° C which is the source of the problem. Motor heat conducted through the motor frame and shaft causes the encoder to skip speed feedback pulses. This creates a false negative slip regenerative braking condition that produced instability in motor torque and would blow the main bus fuses.

Commutation circuit components. - The thermal protection circuit in the controller is activated by temperatures sensed at various components of the commutation circuit. Operating test time for PWM testing was limited by the fast rise in component temperatures in the PWM operating mode. A temperature shutdown required a waiting period for component temperatures to cool below the trip point, and the controller required manual restart of the logic to resume testing.

Audio noise. - Audio noise, due mainly to the commutation transformer core, was present throughout testing. The noise level required the use of ear protectors.

Phase II - Follow-On Design

In a phase II follow-on program to redesign the functional model to an uprated engineering model controller, the power rating was increased approximately 50 percent for diesel equivalent vehicle performance requirements, and the power circuitry was reconfigured to also function as an onboard, integral battery charger. The inverter module package was redesigned for smaller volume, lighter weight, and better thermal management. The use of hockey-puck type SCRs enabled this redesign. Improved components were used to circumvent the problems discussed as test problems. These include 150° C rated semiconductors in the optical speed encoder, low-loss polypropylene capacitors in the commutation circuit, and powdered permalloy magnetic cores for the commutation transformers. The logic and control circuits were redesigned but only to the extent necessary to control and manage the battery-charging function. The engineering model is described in the contractor's final report DOE/NASA/0249-83/1, NASA-CR-168177.

CONCLUDING REMARKS

Road load simulator testing of the Gould phase I functional model controller demonstrated the feasibility of ac motor controllers with state-of-the-art power SCR semiconductors and microprocessor-based logic and control circuits for electric vehicle propulsion systems. The dynamic test results show that this controller has the capability to meet the SAE-J227a schedule D driving cycle requirements for a 1567-kg (3456-lb) vehicle and to accelerate the vehicle to a cruising speed of 88.5 km/hr (55 mph). The regenerative braking capability of the controller (demonstrated in steady state tests) will facilitate reduction in energy per cycle requirements for vehicles by returning braking energy to the battery. The motor and controller combined efficiency during the cruise region of the schedule D cycle is 72 percent and the efficiency of the inverter is 89 percent. These measurements are in agreement with the contractor's reported data. The observed performance improvements for schedule B driving cycle tests with a higher overall gear ratio of 19.68:1 suggests that a two-speed transmission may be beneficial for the schedule D and other driving cycle schedules. A phase II program for an engineering model of the functional model controller uprates the power level for the higher power diesel equivalent performance requirements and incorporates an onboard battery charger within the existing circuitry. The inverter module is redesigned for smaller size, lower weight, and improved thermal management. Improved commutation circuit components and tachometer are used to alleviate thermal and audio noise problems.

The dynamic test results presented in this report provide a base for further development of ac motor controllers for ac propulsion systems for electric vehicles. Further improvements to alleviate the characteristic low-speed stability problems of slip-controlled ac systems are desirable.

APPENDIX A

SAE-J227a SCHEDULES B, C, AND D DRIVING CYCLES AND ROAD LOAD

Driving cycles. - The schedule B, C, and D driving cycles are presented both in tabular and graphical form: Figure 50 and table II define the schedule D during cycle; figure 51 and table III define the schedule C driving cycle; and figure 52 and table IV define the schedule B driving cycle.

Road load. - The road load simulator was adjusted to provide the road loading for a vehicle with the following characteristics and operating on a level road:

Vehicle weight, kg (lb)	1567 (3456)
Tire radius, m (ft)	0.267 (0.875)
Tire rolling resistance, kg/kg (lb/lb) of vehicle weight	0.0095
Aerodynamic drag coefficient (Cd)	0.046
Frontal area, m^2 (ft^2)	1.82 (19.6)
Air density (P), kg/m^3 ($slug/ft^3$)	1.226 (0.00238)

The road load torque provided by the RLS for vehicle speeds up to 88.5 km/hr (55 mph) is shown by the characteristic road load curve in figure 53. The corresponding road load torque reflected to the motor through the transaxle set for the overall gear ratio of 8.22:1 is shown in figure 54. The motor shaft horsepower required for the road loading is shown in figure 55.

APPENDIX B

STEADY STATE TEST RESULTS - CONSTANT TORQUE MOTORING MODE

Steady state tests were run at constant motor load torque by operating the RLS as a conventional dynamometer. Torque loading was held constant by the RLS torque control loop, motor speed was varied by means of the accelerator potentiometer on the controller, and dc power was obtained from the battery simulator supply.

Motor controller efficiency. - A composite set of curves of combined motor controller system efficiency as a function of motor speed for a range of constant torque loads is shown in figure 56. Torque loads ranged from 2.82 to 16.95 Nm (25 to 150 in-lb) for a dc supply of 120 V, and from 16.95 to 59.3 Nm (150 to 525 in-lb) for a voltage of 132 V. Motor speed was varied from 0 to 785 rad/sec (7500 rpm). The curves show a predominant inflection at light torque loading for a motor speed range from approximately 262 to 471 rad/sec (2500 to 4500 rpm). This speed range corresponds to the transition region described in the report where the controller's operating mode changes from PWM to quasi-square wave operation. The motor current and voltage waveform photographs in figure 57 illustrate this transition. The upper traces in the photographs are motor phase currents and the lower traces are motor line to line voltages. At a motor speed of 111 rad/sec (1060 rpm) the operating mode is PWM with many commutations per cycle, and at 523 rad/sec (4995 rpm) the operation is quasi-square wave with only 2 turnoff commutations per half cycle. The transition interval is approximately at the midpoint at 368 rad/sec (3514 rpm) and is nearly complete at 452 rad/sec (4316 rpm). Notches in the voltage waveforms result from the bus commutation technique to switch the power SCR semiconductors.

The results in figure 56 conform with the results reported by the contractor in his final report, NASA CR-167919. The inflections correlate with the torque and power dips reported, and the efficiencies are in agreement with the efficiency map.

Steady state characteristics at 34 Nm (300 in-lb). - Steady state characteristic curves of individual parameters for a constant motor load torque of 34 Nm (300 in-lb) and variable motor speed for a dc supply of 105 and 132 V are shown in figures 58 to 64. These curves provide some detail of the magnitudes of the individual parameters and the effects of the supply voltage. The following parameters are shown as a function of motor speed in figures 58 to 64: inverter efficiency, motor efficiency, battery power, battery current, motor voltage, motor current, and slip frequency.

APPENDIX C

STEADY STATE TEST RESULTS - CONSTANT SPEED MOTORING MODE

Steady state tests were run at constant motor speed and variable motor torque loading by operating the RLS as a conventional dynamometer. Motor speed was held constant by the speed control loop of the RLS and torque was varied in discrete steps by the accelerator potentiometer in the controller. Test motor speeds varied from 35.6 to 785.3 rad/sec (340 to 7500 rpm) and the motor torque loads were varied to 70.6 Nm (625 in-lb).

The test results are shown as a family of characteristic curves for each parameter. The following parameters presented in figures 65 to 70 are as follows: motor controller combined efficiency, motor voltage, motor current, battery current, inverter output frequency, and slip frequency.

APPENDIX D

STEADY STATE TEST RESULTS - CONSTANT TORQUE

Regeneration mode. - Steady state regenerative mode tests were run with the RLS operated as a conventional dynamometer. Direct current power for the controller and motor system was obtained from a battery supply that was initially conditioned to a 40-percent state-of-charge level. Negative torque loading was held constant at discrete levels over a torque range of -16.9 to -59.3 Nm (-150 to -525 in-lb). Motor speed was varied over a speed range of 161 to 785 rad/sec (1540 to 7500 rpm). Regeneration of the functional model controller is ineffective at motor speeds less than 161 rad/sec (1540 rpm).

Motor controller efficiency. - A composite set of curves of combined motor controller system efficiency as a function of motor speed for the above range of negative torque loads is shown in figure 71. This set of curves shows the same inflection in the efficiency curve at light loads that was obtained in the motoring mode (see appendix B) over the controller's transition interval from PWM to quasi-square wave operating mode. The individual efficiency curves overall are in agreement with the efficiency curves for the motoring mode of motor operation shown in appendix B.

Family of curves. - Characteristic families of curves for the individual parameters are shown in figures 72 to 78. The following parameters are presented: motor shaft power in kilowatts, motor voltage, motor current, battery current, battery voltage, battery power, and slip frequency.

REFERENCES

1. Sargent, Noel B.: A Laboratory Facility For Electric Vehicle Propulsion System Testing. NASA TM-81574, 1980
2. Latos, Thomas S.: Improved SCR-AC Motor Controller for Battery Powered Urban Electric Vehicles. (Rept-815-008, Gould, Inc.; NASA Contract DEN 3-60.) NASA CR-167919, DOE/NASA/0060-82/1, 1982
3. Stenger, Francis J.: Tests of an Alternating Current Propulsion Subsystem for Electric Vehicles on a Road Load Simulator. NASA TM-83036, DOE/NASA/51044-29, 1982.
4. Geppert, Steven: AC Propulsion System for an Electric Vehicle, Phase I (ERC-TR-8101, Eaton Engineering and Research Center; NASA Contract DEN 3-125.) NASA CR-165480, DOE/NASA/0125-1, 1981.

TABLE I. - INSTRUMENT LIST

Test parameter	Symbol	Instrument	Range
Battery voltage	VB	Fluke DVM, rms	0-200 V
Motor voltages:			
Lines 1-2	VM(1-2)		
Lines 2-3	VM(2-3)		
Lines 3-1	VM(3-1)		
Battery current	IB	Coaxial shunt and fluke DVM, rms	250 amps, rms
Motor currents:			
Phase 1(φ_1)	IM-1		
P[ase 2(φ_2)	IM-2		
Phase 3(φ_3)	IM-3		
Battery power:	PB	Clark-Hesse wattmeter	Varies with shunt
Inverter output power:			
Phase 1	PI-1		
Phase 2	PI-2		
Phase 3	PI-3		
Inverter output frequency	fI	Special D/A circuit	0-300 Hz
Motor slip frequency	fSL	Special D/A circuit	0-10 Hz
Motor rotor frequency	fMR	Lebow torque/speed meter	0-800 rpm and 0-300 Hz
Motor output torque	TQM	Lebow torque meter	0-1000 in-lb
Vehicle wheel torque	TQV	Lebow torque meter	0-9000 in-lb
Motor shaft speed	SM	Lebow torque/speed meter	0-8000 rpm
Vehicle wheel rotational speed	SV	Lebow torque/speed meter	0-1000 rpm
Commutating capacitor temperature	TI-CAP	Thermocouple	200° F
Inverter internal temperature (ambient)	TI-AMB		200° F
Motor temperature	TM-1		400° F
Motor temperature	TM-2		400° F
Motor temperature	TM-3		400° F

TABLE II. - SCHEDULE D

Time, sec	Speed, mph	Time, sec	Speed, mph	Time, sec	Speed, mph
0	0	25	43.31	91	19.00
1	2.56	26	43.93	92	15.83
2	5.12	27	44.49	93	12.67
3	7.68	28	45.00	94	9.50
4	10.24	29	45.00	95	6.33
5	12.80	30	45.00	96	3.17
6	15.36	--	-----	97	0
7	17.79	75	45.00	[a]98	0
8	20.08	76	45.00	99	0
9	22.24	77	45.00	100	0
10	24.28	[a]78	45.00	---	-----
11	26.20	79	43.53	120	0
12	28.01	80	42.33	121	0
13	29.72	81	41.33	[a]122	(b)
14	31.34	82	40.40		
15	32.85	83	39.53		
16	34.27	84	38.73		
17	35.60	[a]85	38.00		
18	36.85	86	34.83		
19	38.01	87	31.67		
20	39.09	88	28.50		
21	40.08	89	25.33		
22	41.00	90	22.17		
23	41.85				
24	42.61				

[a] Denotes transition points from one mode to another (i.e., acceleration to cruise, etc.).

[b] Repeated cycle starting at 9 sec.

TABLE III. - SCHEDULE C

Time, sec	Speed, mph	Time, sec	Speed, mph	Time, sec	Speed, mph
0	0	21	30.00	54	2.89
1	2.65	--	-----	[a]55	0
2	5.31	37	30.00	56	
3	7.97	[a]38	30.00	57	
4	10.60	39	29.19	58	
5	13.05	40	28.45	59	
6	15.28	41	27.89	60	
7	17.33	42	27.40	--	----
8	19.18	43	26.98	78	0
9	20.89	44	26.59	79	0
10	26.98	78	26.27	[a]80	(b)
11	23.83	46	26.00		
12	25.08	47	23.11		
13	26.21	48	20.22		
14	27.20	49	17.33		
15	28.07	50	14.44		
16	28.82	51	11.56		
17	29.45	52	8.67		
[a]18	30.00	53	5.78		
19	30.00				
20	30.00				

[a] Denotes transition points from one mode to another (i.e., acceleration to cruise etc.).

[b] Repeat cycle starting at 9 sec.

TABLE IV. - SCHEDULE B

Time, sec	Speed, mph	Time, sec	Speed, mph	Time, sec	Speed, mph
0	0	21	20.00	51	0
1	1.67	22	20.00	52	0
2	3.35	--	-----	--	---
3	5.03	36	20.00	70	0
4	6.71	[a]37	20.00	71	0
5	8.28	38	20.00	[a]72	(b)
6	9.78	39	19.20		
7	11.06	40	18.60		
8	12.28	[a]41	18.20		
9	13.40	42	18.00		
10	14.43	43	14.40		
11	15.36	45	7.20		
12	16.20	[a]46	3.60		
13	16.97	47	0		
14	17.65	48	0		
15	18.26	49	0		
16	18.80	50	0		
17	19.26				
18	19.66				
[a]19	20.00				
20	20.00				

[a] Denotes transition points from one mode to another (i.e., acceleration to cruise etc.).
[b] Repeat cycle starting at 9 sec.

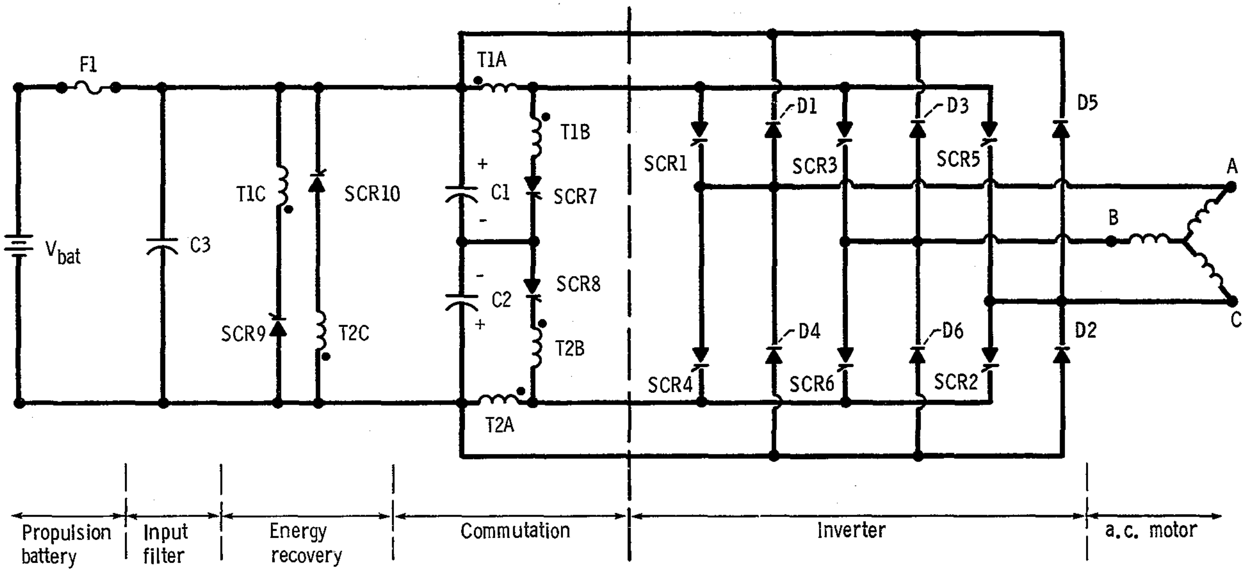

Figure 1. - Electric vehicle propulsion system power stage configuration.

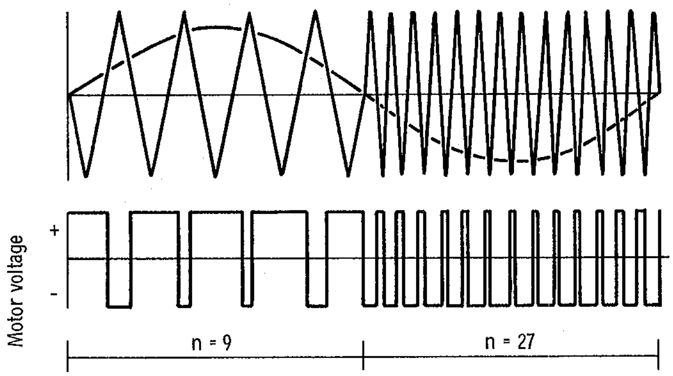

Figure 2. - Sine triangle modulation strategy showing effect of changing triangle/ sine ratio parameter n. (For n = 9, the first significant motor harmonic is the 17th; for n = 27, this changes to the 53rd. Developed motor terminal voltage is independent of n but varies with the relative amplitudes of sine and triangle ref reference waveforms.

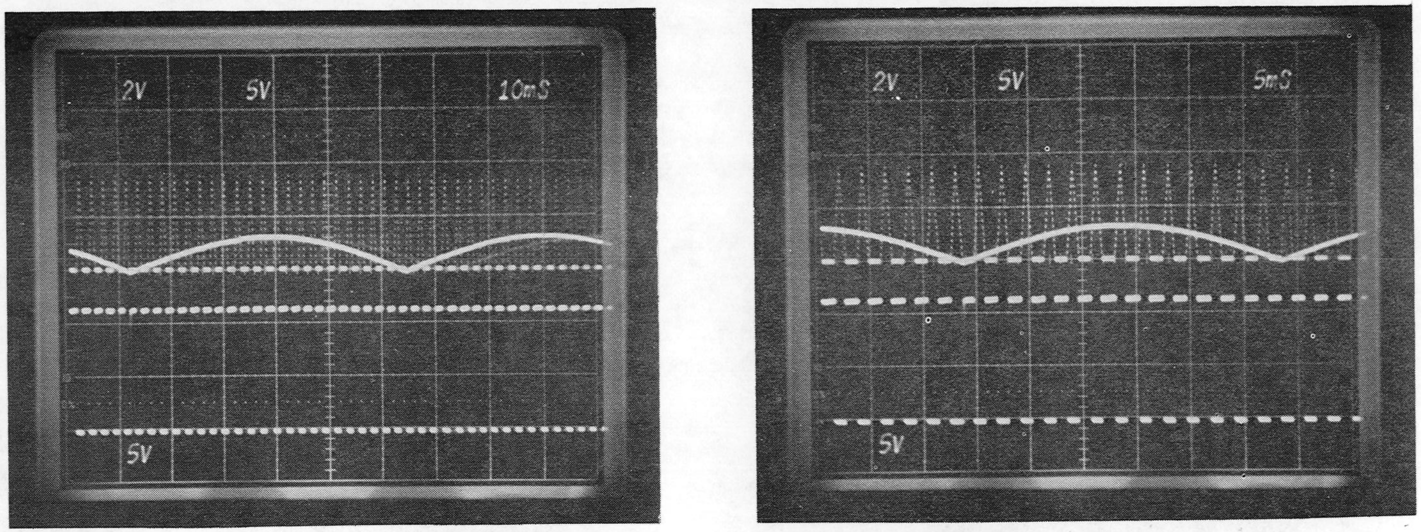

(a) High ratio motor speed, 240 rpm.

(b) Medium ratio motor speed, 507 rpm.

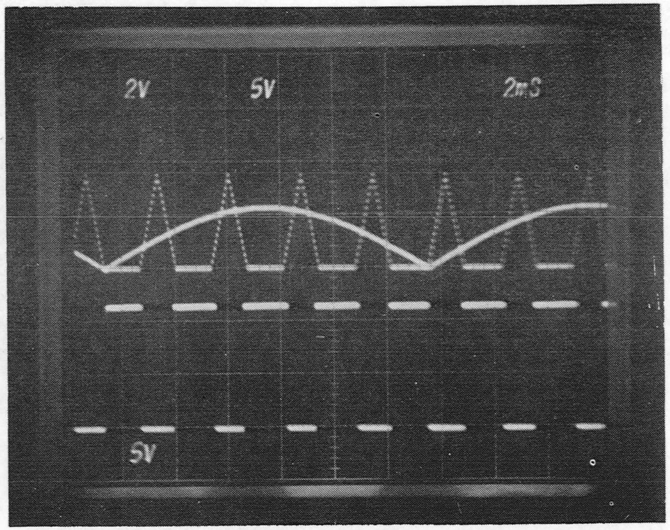

(c) Low ratio motor speed, 1240 rpm.

Figure 3. - Sine-triangle ratio and PWM pulse drive waveforms.

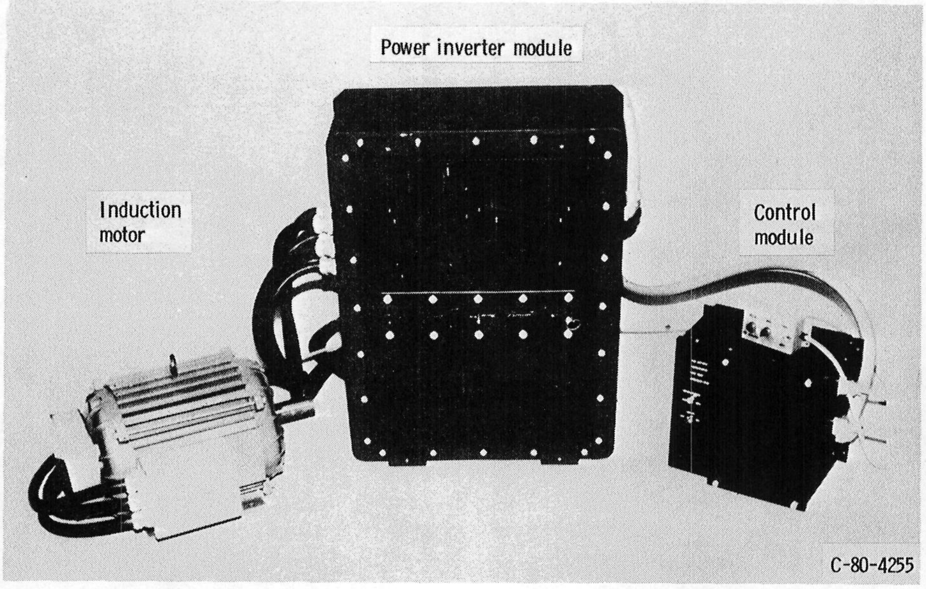

Figure 4. - Functional model ac controller and motor system.

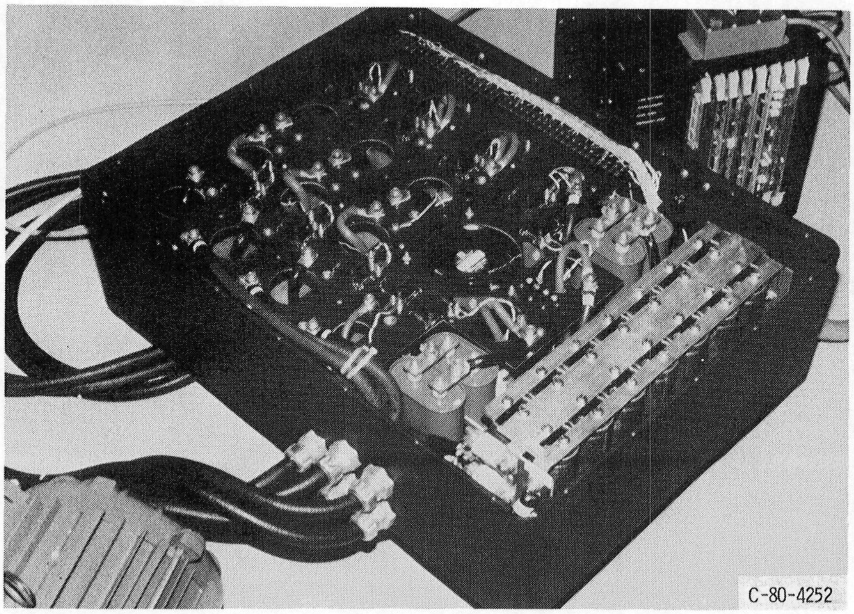

Figure 5. - Internal view of inverter and control modules.

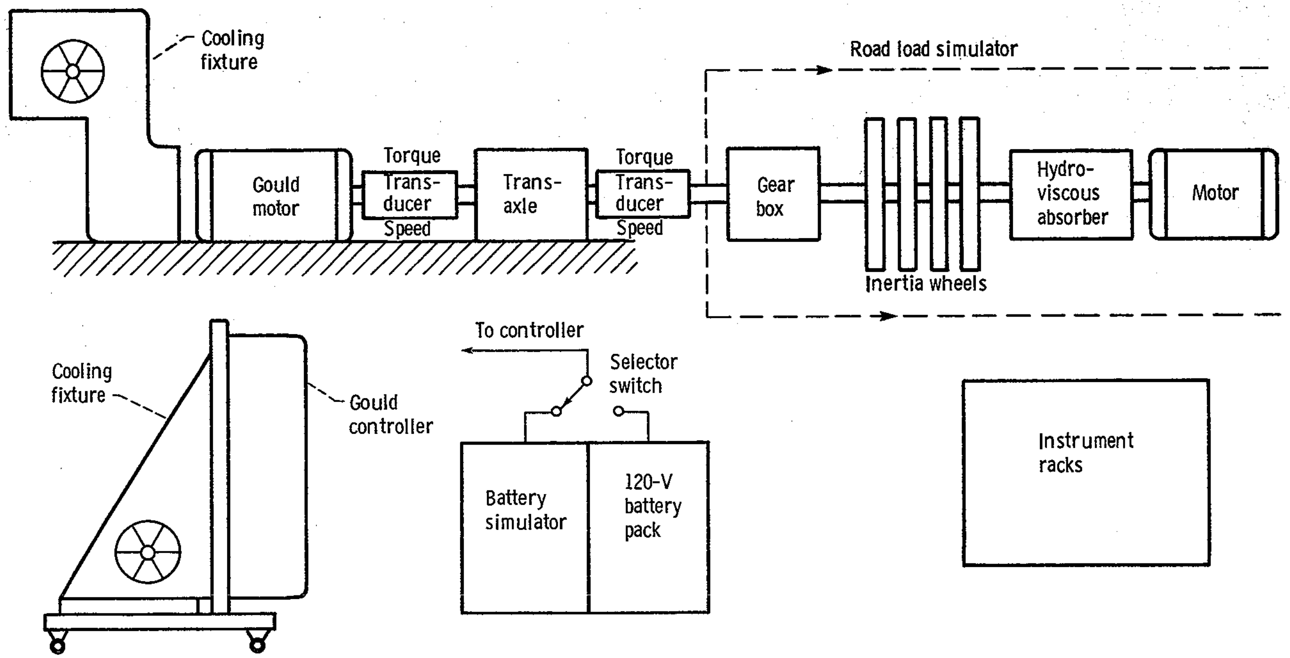

Figure 6. - Test layout for road load simulator (RLS) tests of Gould a.c. motor controller with transaxle.

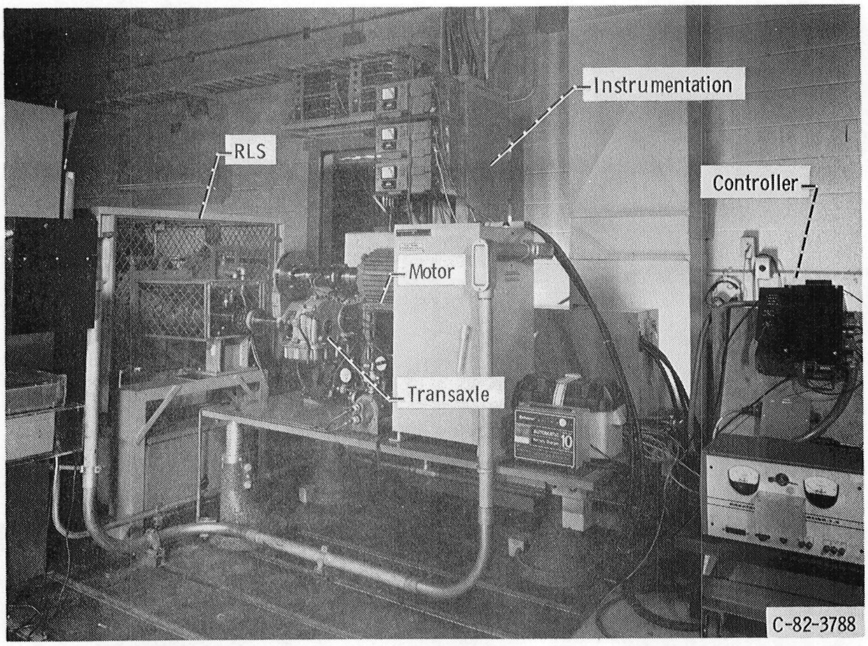

Figure 7. - Road load simulator test of functional model controller, load motor, and transaxle.

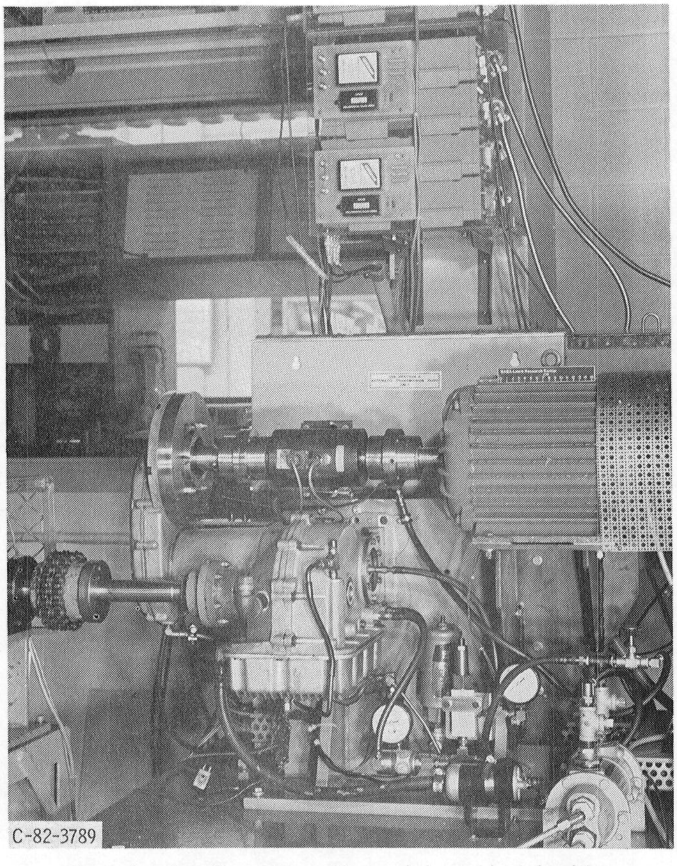

Figure 8. - Coupling motor and transaxle to road load simulator.

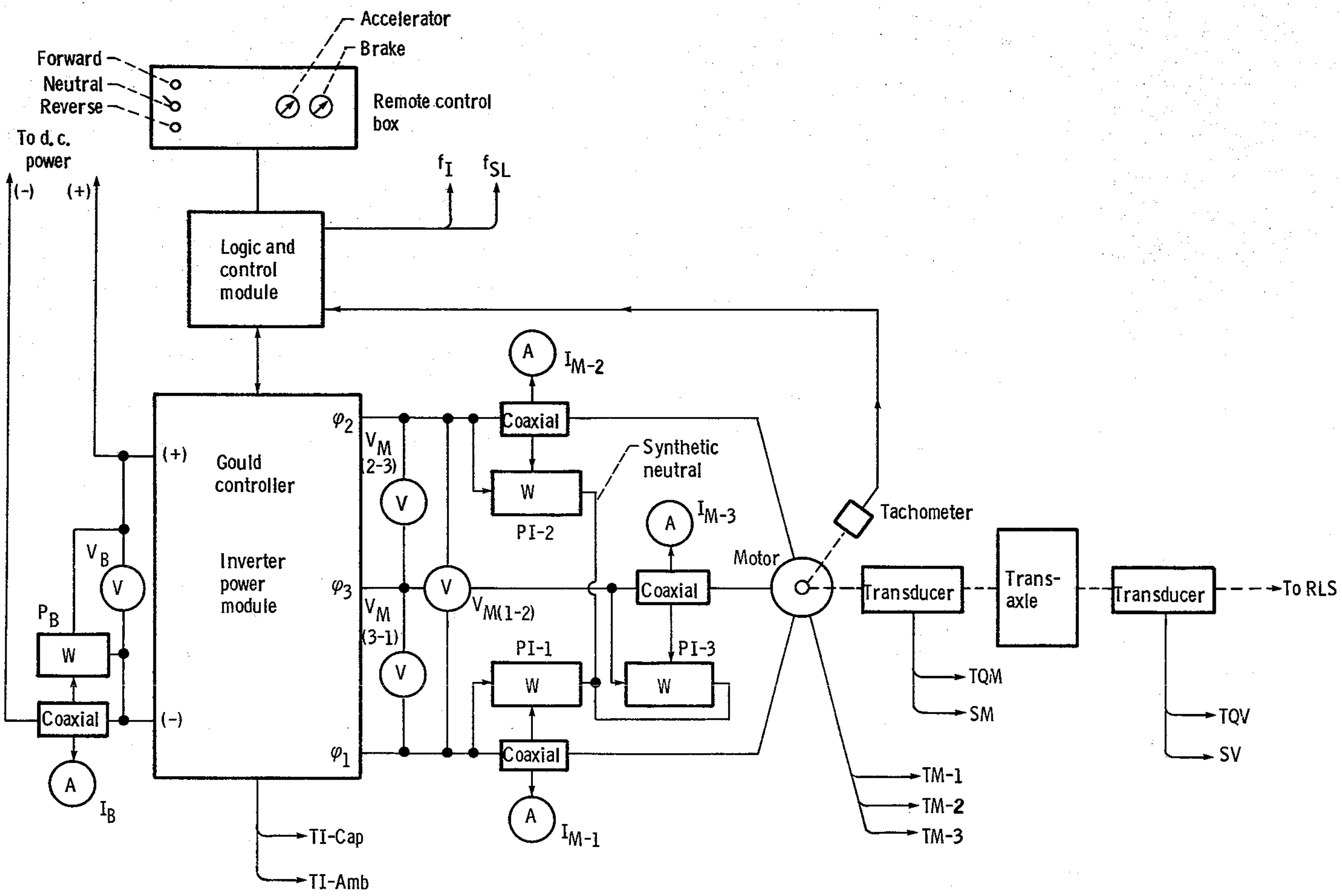

Figure 9. - Instrument and wiring layout for road load simulator tests of Gould a. c. motor controller.

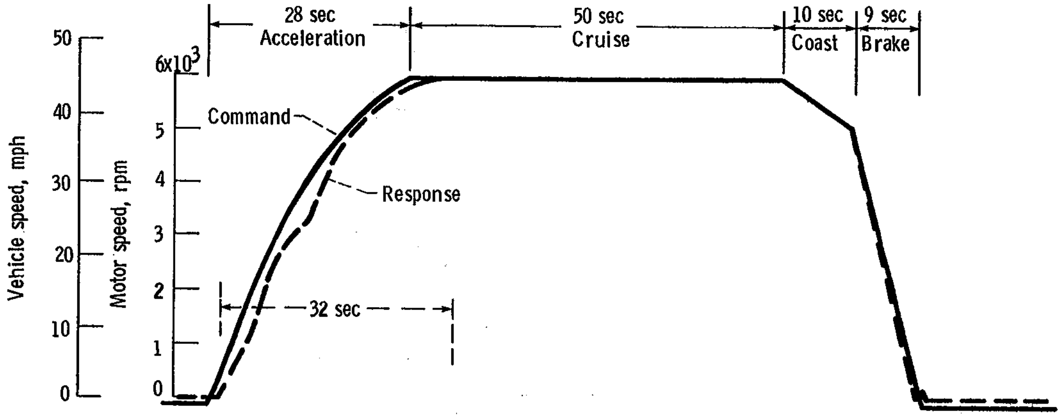

Figure 10. - D cycle test. Gear ratio, 8.22.

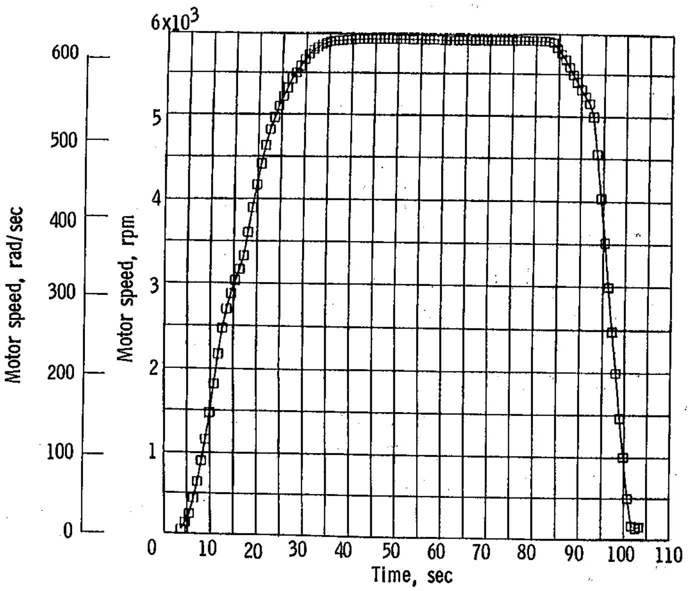

Figure 11. - Motor speed as function of time for SAE-J227a schedule D cycle. Gear ratio, 8.22.

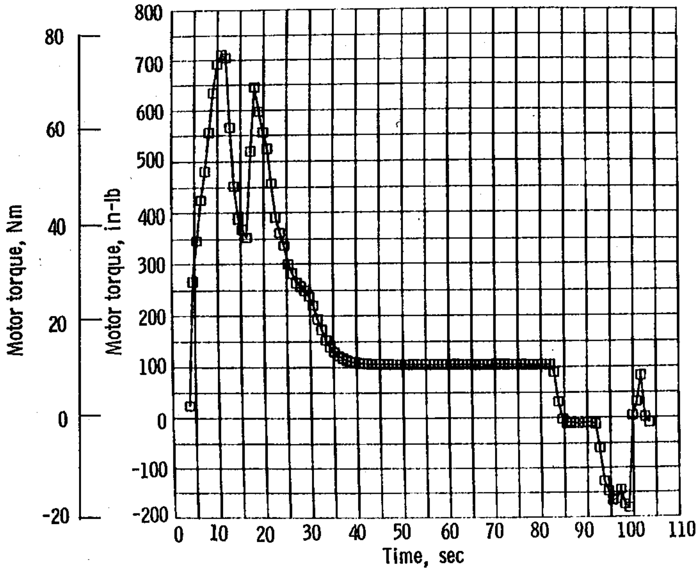

Figure 12. - Motor torque as function of time for SAE-J227a schedule D cycle. Gear ratio, 8.22.

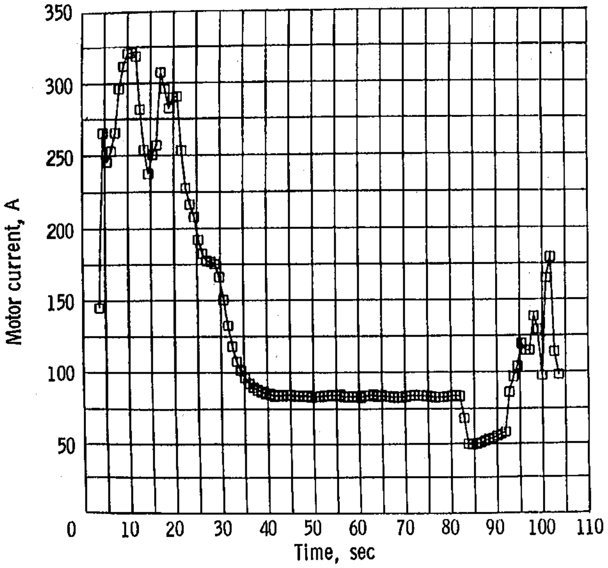

Figure 13. - Motor current as function of time for SAE-J227a schedule D cycle. Gear ratio, 8.22.

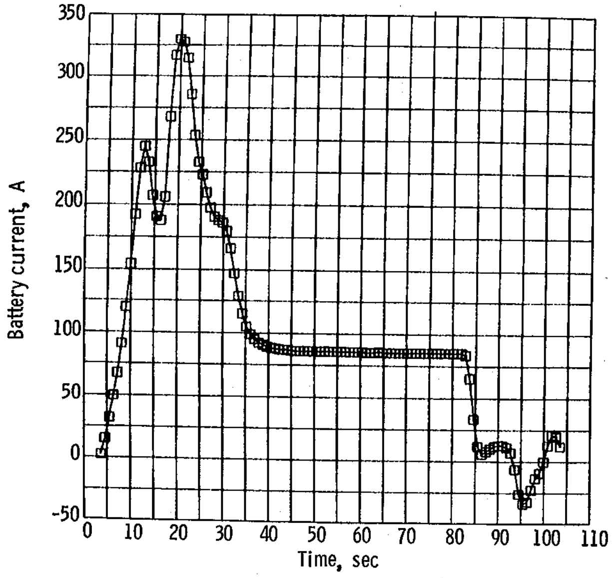

Figure 14. - Battery current as function of time for SAE-J227a schedule D cycle. Gear ratio, 8.22.

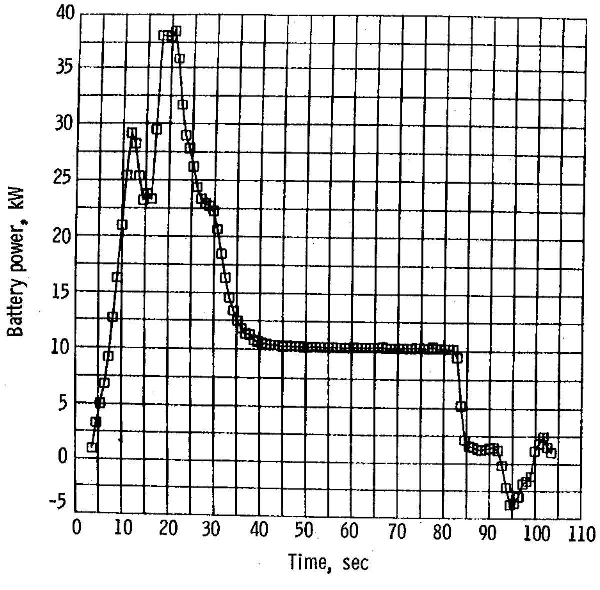

Figure 15. - Battery power as function of time for SAE-J227a schedule D cycle. Gear ratio, 8.22.

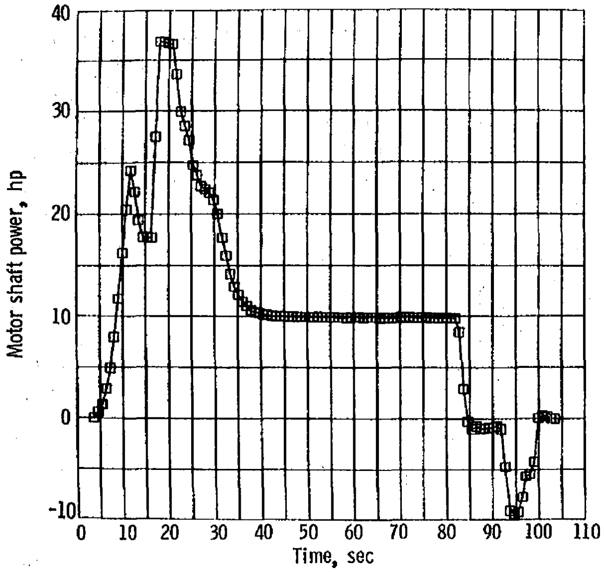

Figure 16. - Motor shaft power as function of time for SAE-J227a schedule D cycle. Gear ratio, 8.22.

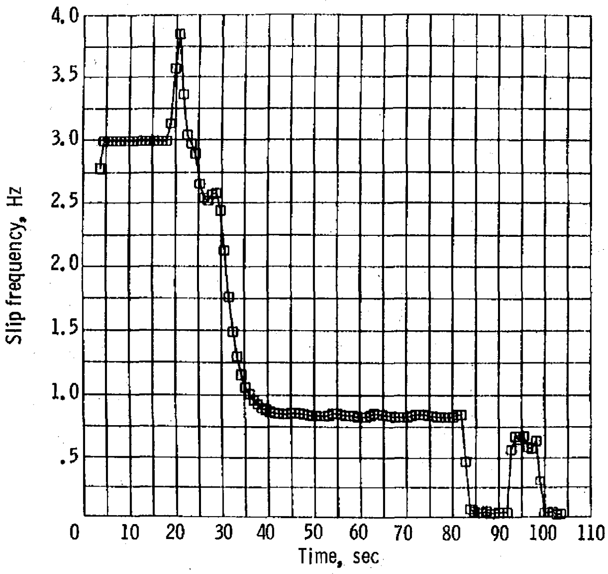

Figure 17. - Slip frequency as function of time for SAE-227a schedule D cycle. Gear ratio, 8.22.

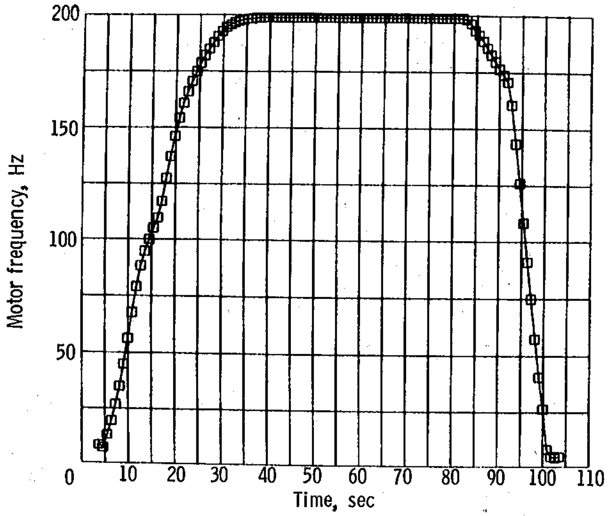

Figure 18. - Motor excitation frequency as function of time for SAE-J227a schedule D cycle. Gear ratio, 8.22.

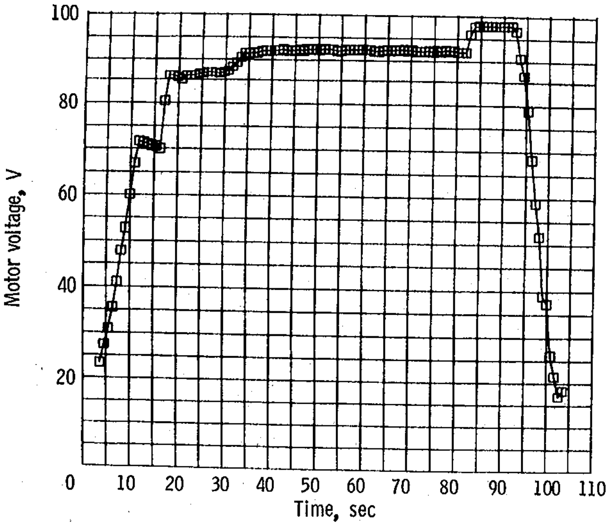

Figure 19. - Motor line voltage as function of time for SAE-J227a schedule D cycle. Gear ratio, 8.22.

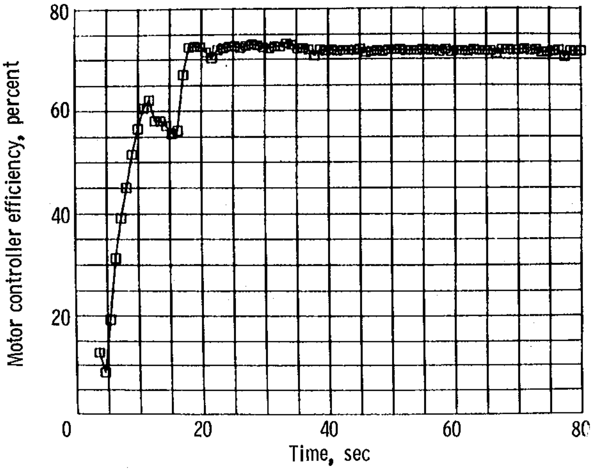

Figure 20. - Motor controller system efficiency as function of time for SAE-J227a schedule D cycle. Gear ratio, 8.22.

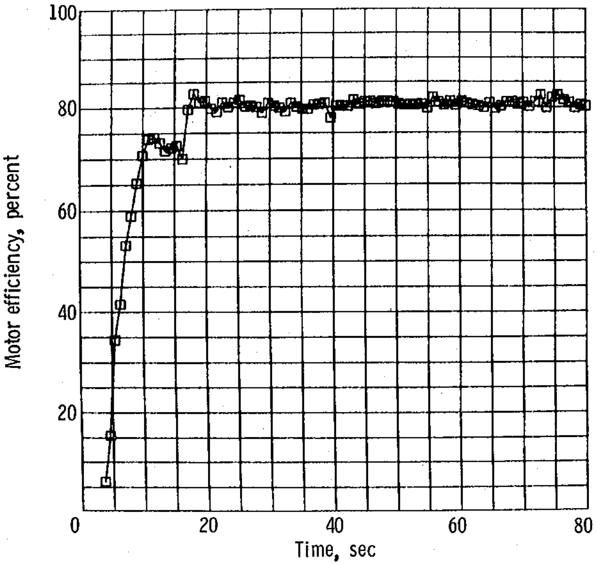

Figure 21. - Motor efficiency as function of time for SAE-J227a schedule D cycle. Gear ratio, 8.22.

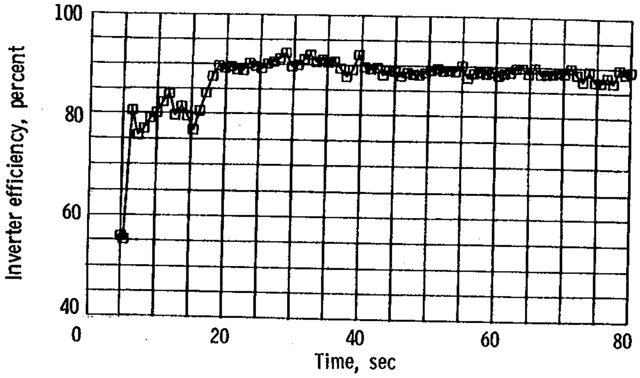

Figure 22. - Inverter efficiency as function of time for SAE-J227a schedule D cycle. Gear ratio, 8.22.

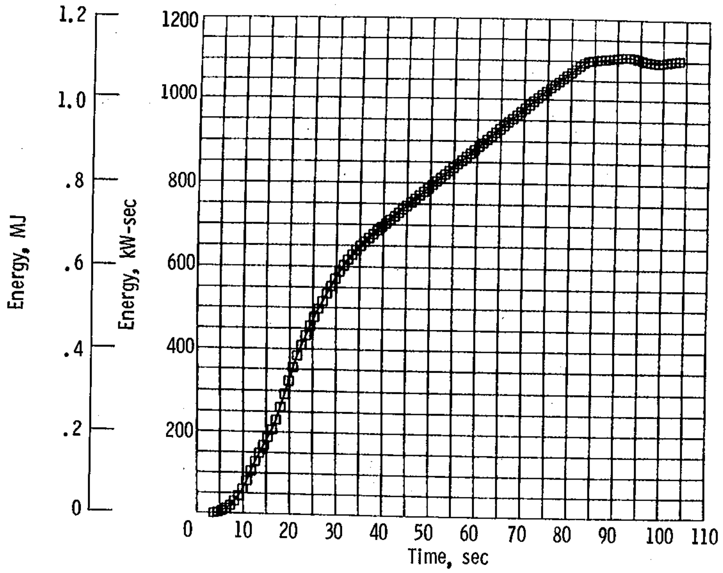

Figure 23. - Energy requirement as function of time for SAE-J227a schedule D cycle. Gear ratio, 8.22.

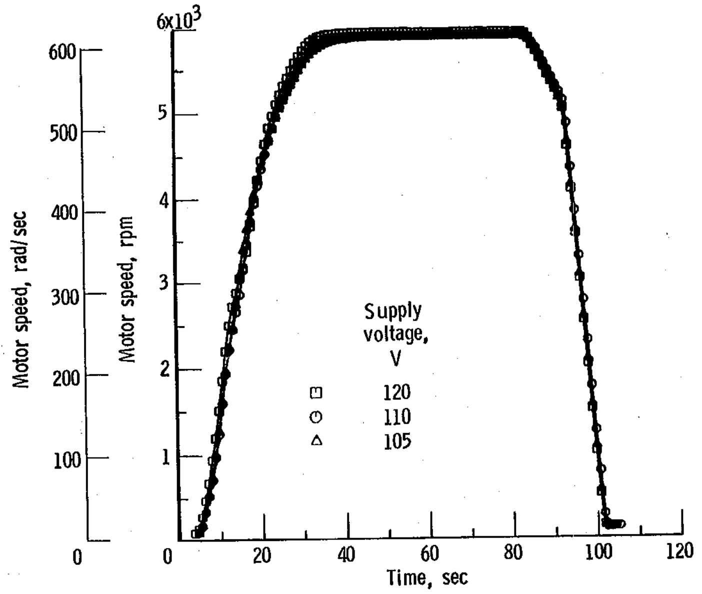

Figure 24. - Effect of supply voltage on motor speed response for SAE-J227a schedule D cycle. Gear ratio, 8.22.

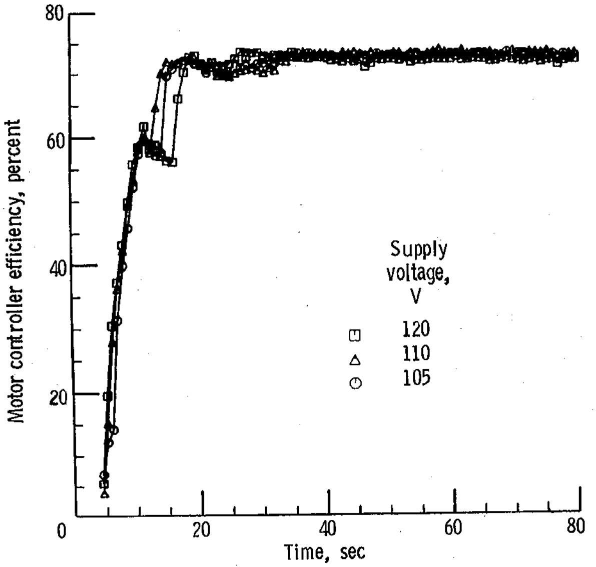

Figure 25. - Effect of supply voltage on motor controller efficiency for SAE-J227a schedule D cycle. Gear ratio, 8.22.

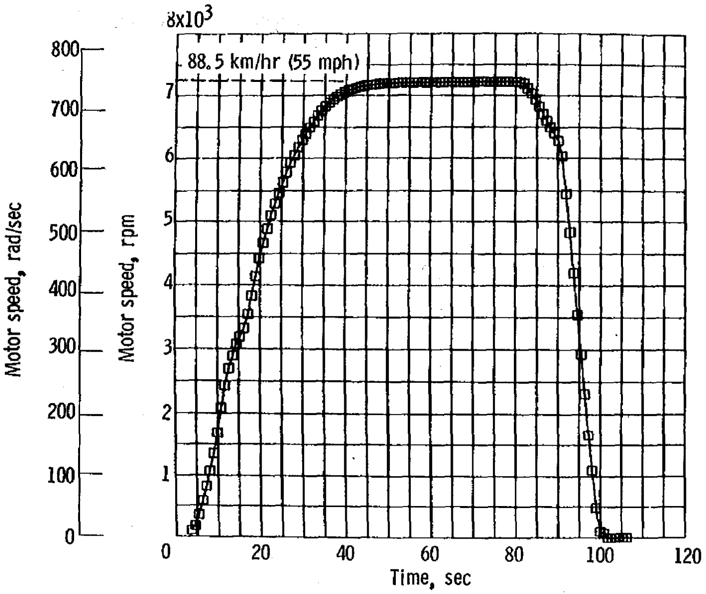

Figure 26. - Motor speed as function of time for maximum vehicle acceleration to 88.5 km/hr (55 mph). Gear ratio, 8.22; battery terminal voltage, 120 V.

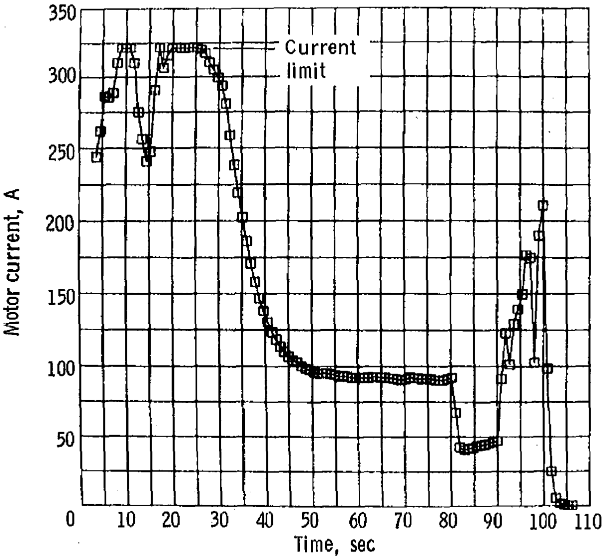

Figure 27. - Motor current as function of time for maximum vehicle acceleration to 88.5 km/hr (55 mph). Gear ratio, 8.22; battery terminal voltage, 120 V.

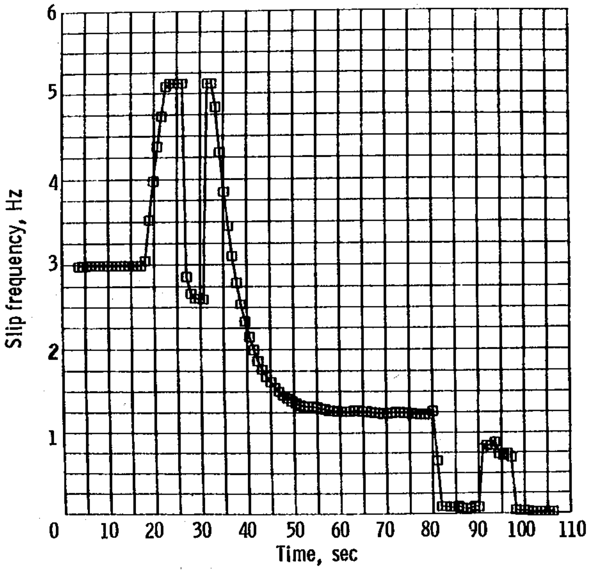

Figure 28. - Slip frequency as function of time for maximum vehicle acceleration to 88.5 km/hr (55 mph). Gear ratio, 8.22; battery terminal voltage, 120 V.

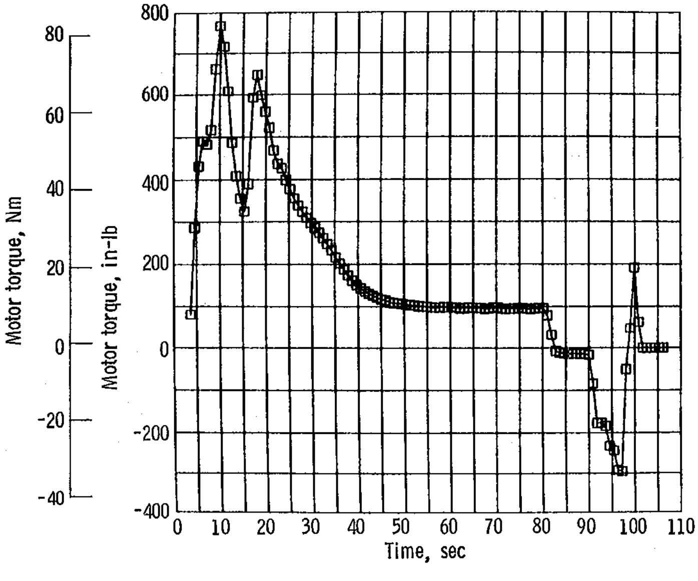

Figure 29. - Motor torque as function of time for maximum vehicle acceleration to 88.5 km/hr (55 mph). Gear ratio, 8.22; battery terminal voltage, 120 V.

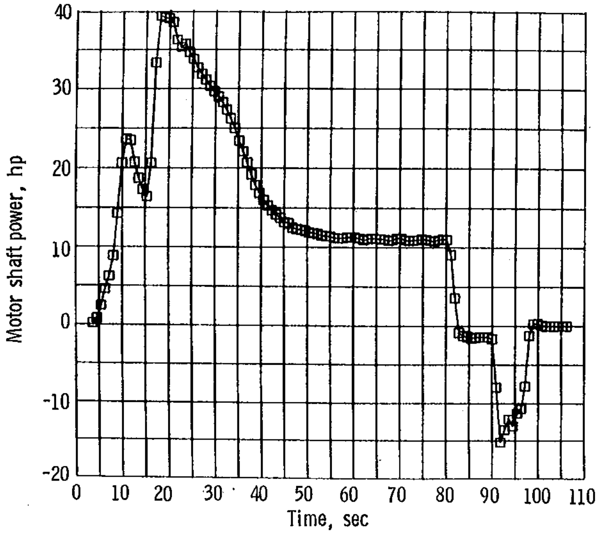

Figure 30. - Motor shaft power as function of time for maximum vehicle acceleration to 88.5 km/hr (55 mph). Gear ratio, 8.22; battery terminal voltage, 120 V.

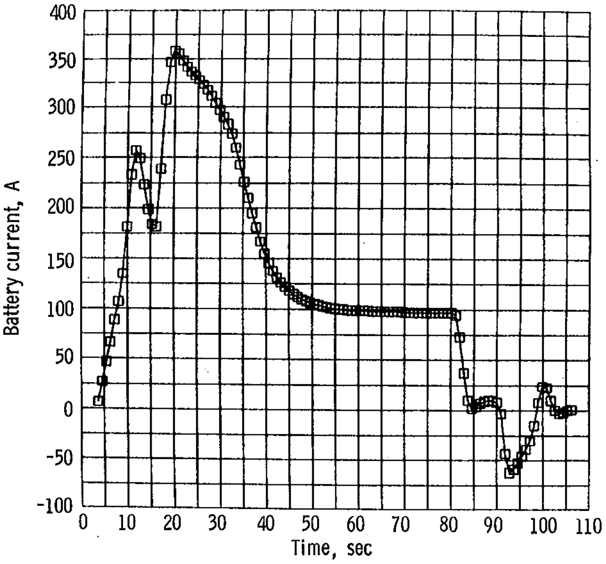

Figure 31. - Battery current as function of time for maximum vehicle acceleration to 88.5 km/hr (55 mph). Gear ratio, 8.22; battery terminal voltage, 120 V.

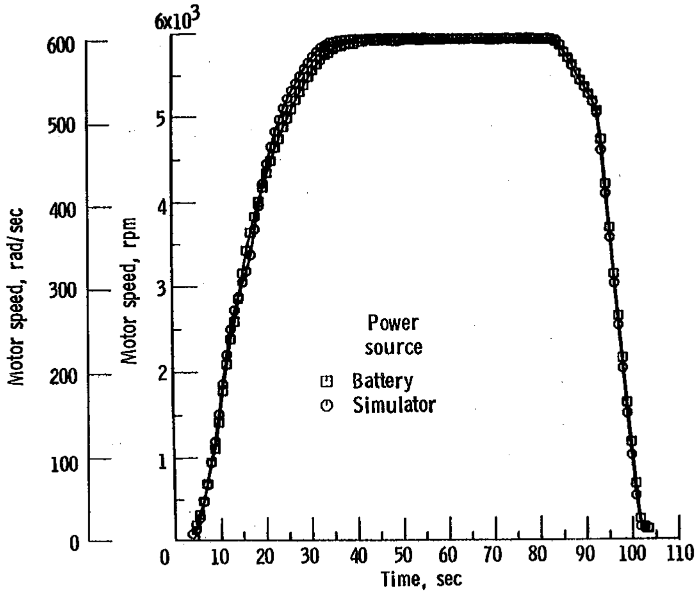

Figure 32. - Effect of power sources on motor speed as function of time response for SAE-J227a schedule D cycle. Gear ratio, 8.22.

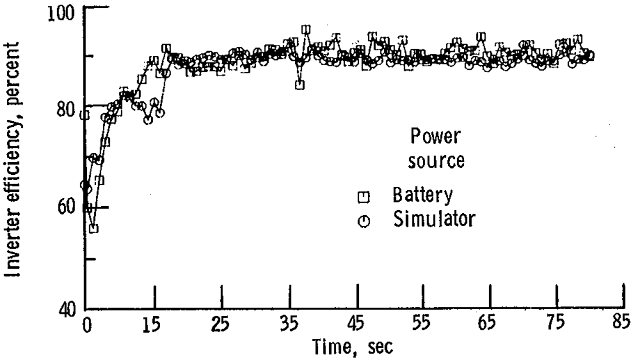

Figure 33. - Effect of power sources on inverter efficiency for SAE-J227a schedule D cycle. Gear ratio, 8.22.

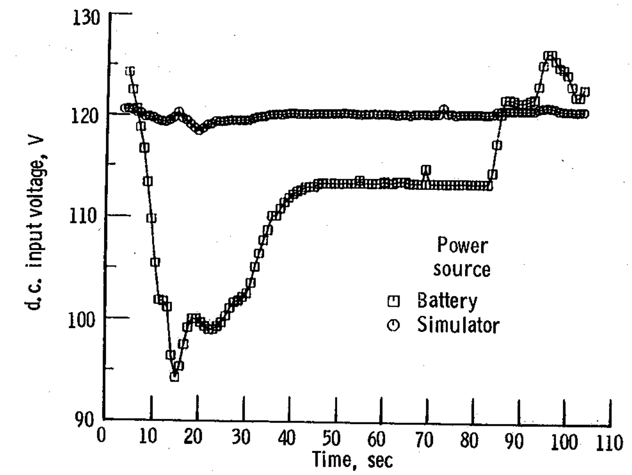

Figure 34. - Effect of power sources on d.c. input voltage for SAE-J227a schedule D cycle. Gear ratio, 8.22.

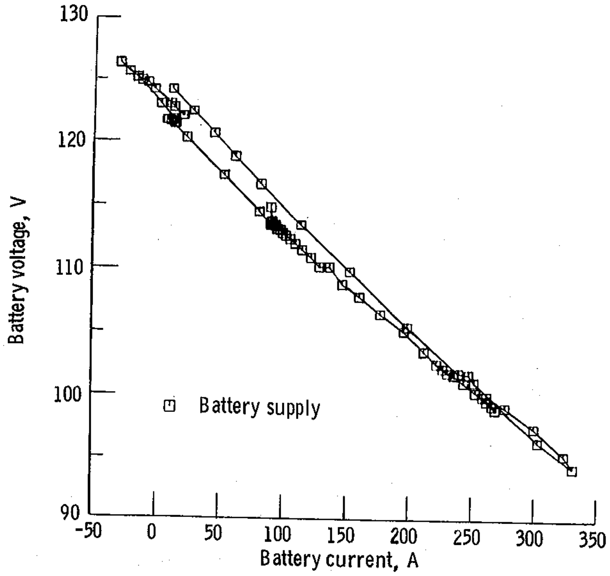

Figure 35. - Voltage current characteristic of battery supply for SAE-J227a schedule D cycle. Gear ratio, 8.22; battery supply's internal impedance (Z_{int}), 0.10 ohm.

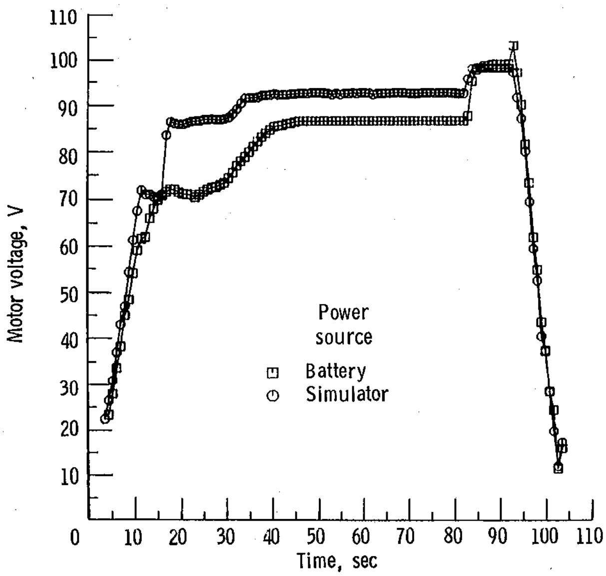

Figure 36. - Effect of power sources on motor voltage for SAE-J227a schedule D cycle. Gear ratio, 8.22.

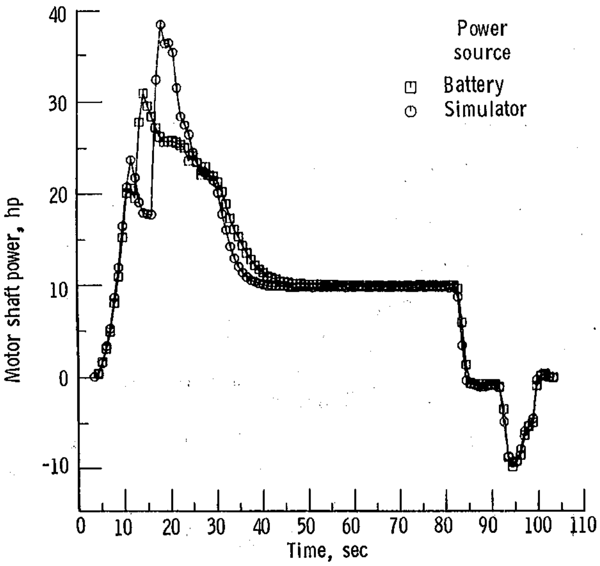

Figure 37. - Effect of power sources on motor shaft power for SAE-J227a schedule D cycle. Gear ratio, 8.22.

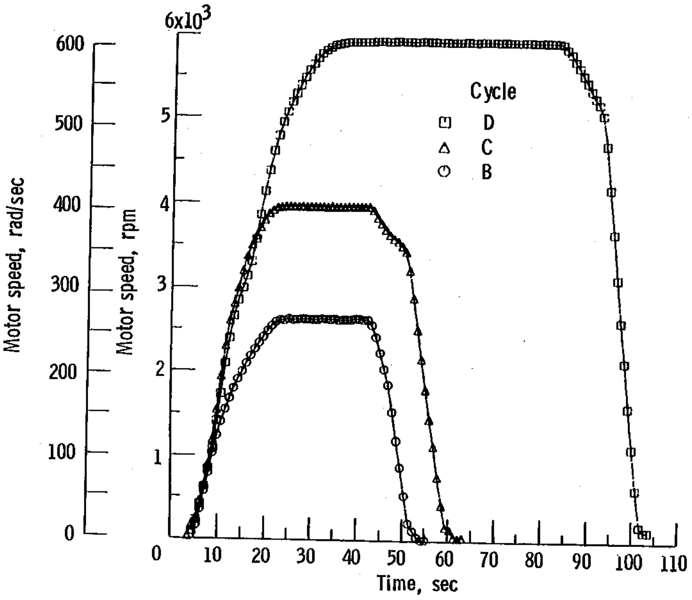

Figure 38. - Motor speed as function of time for SAE-J227a schedules B, C, and D. Gear ratio, 8.22.

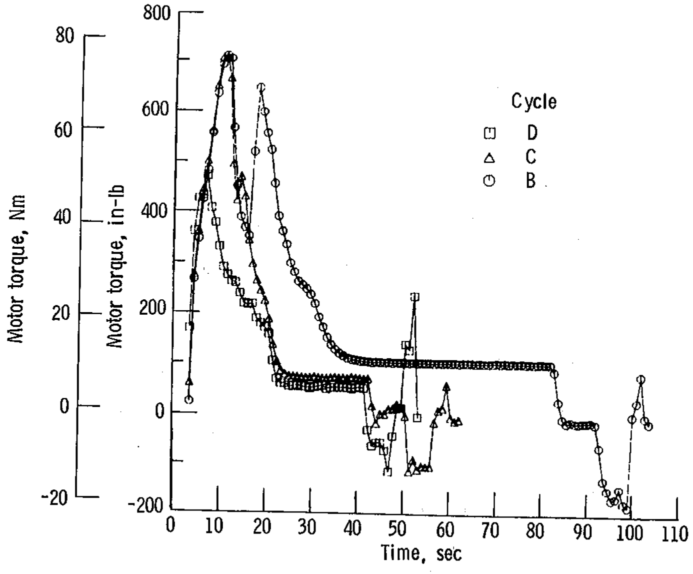

Figure 39. - Motor torque as function of time for SAE-J227a schedules B, C, and D. Gear ratio, 8.22.

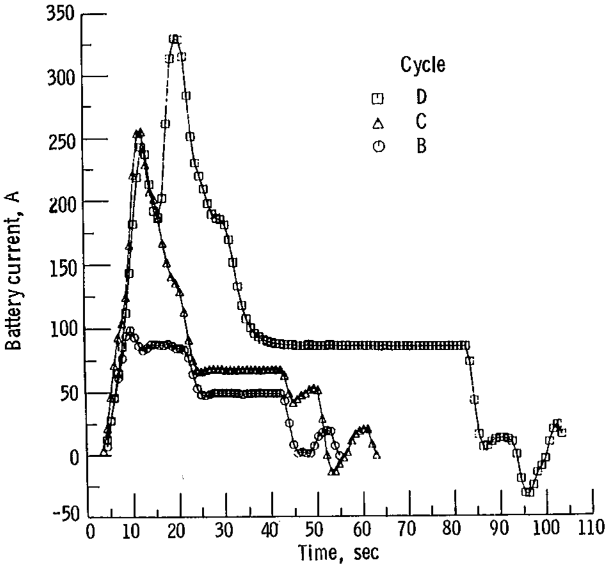

Figure 40. - Battery current as function of time for SAE-J227a schedules B, C, and D. Gear ratio, 8.22.

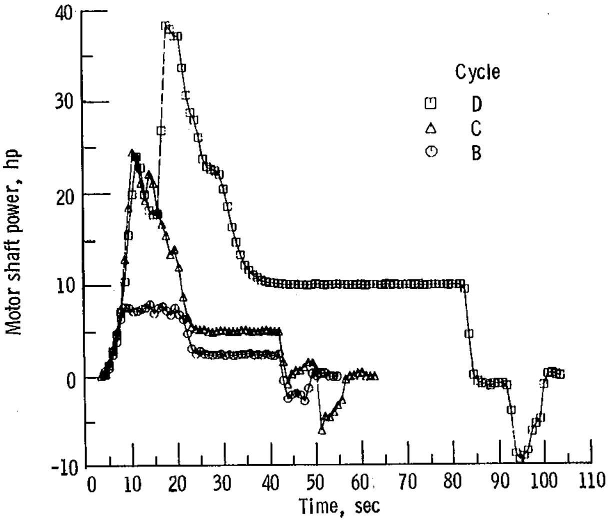

Figure 41. - Motor shaft power as function of time for SAE-J227a schedules B, C, and D. Gear ratio, 8.22.

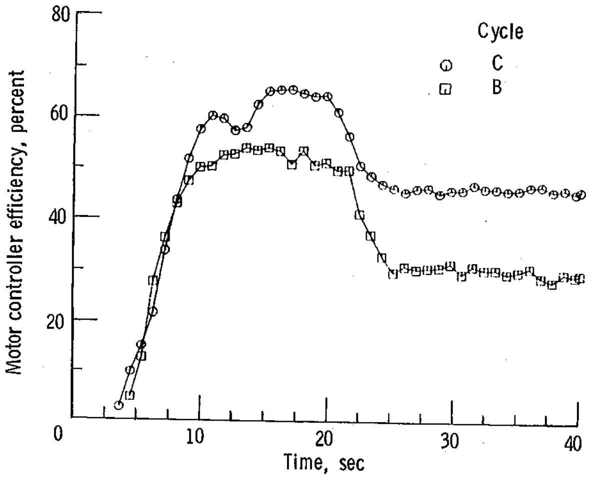

Figure 42. - Motor controller system efficiency as function of time for SAE-J227a schedules B and C. Gear ratio, 8.22.

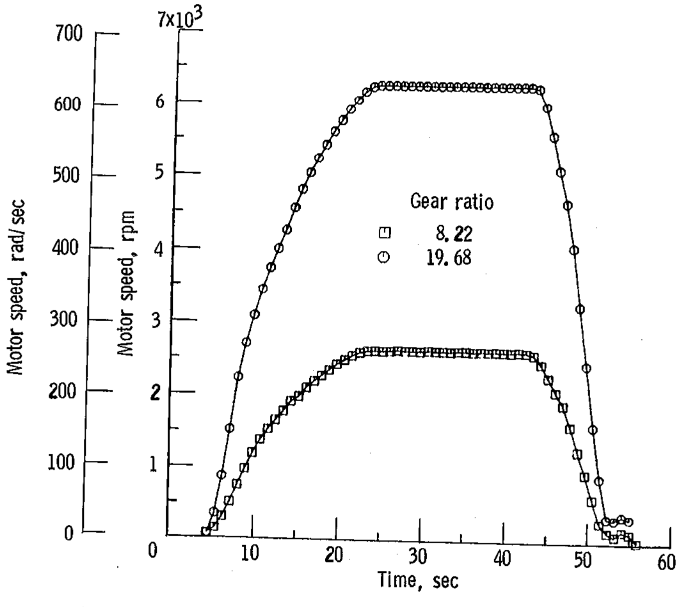

Figure 43. - Motor speed as function of time for two gear ratios for SAE-J227a schedule B cycle.

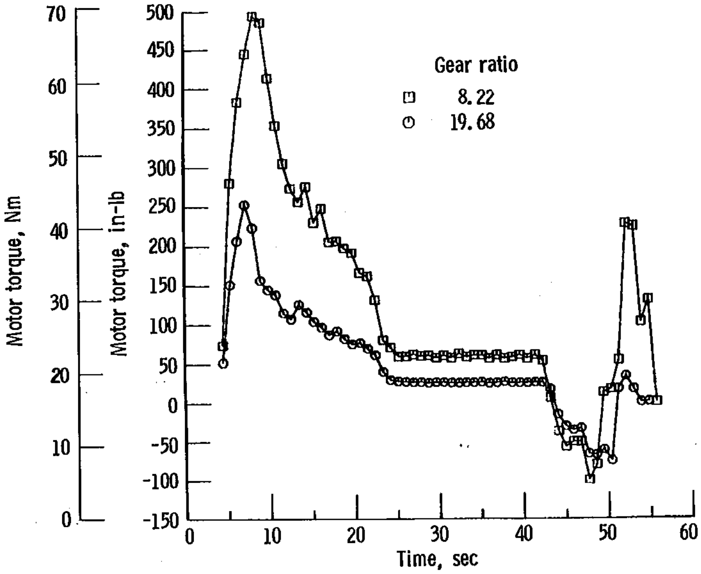

Figure 44. - Motor torque as function of time for two gear ratios for SAE-J227a schedule B cycle.

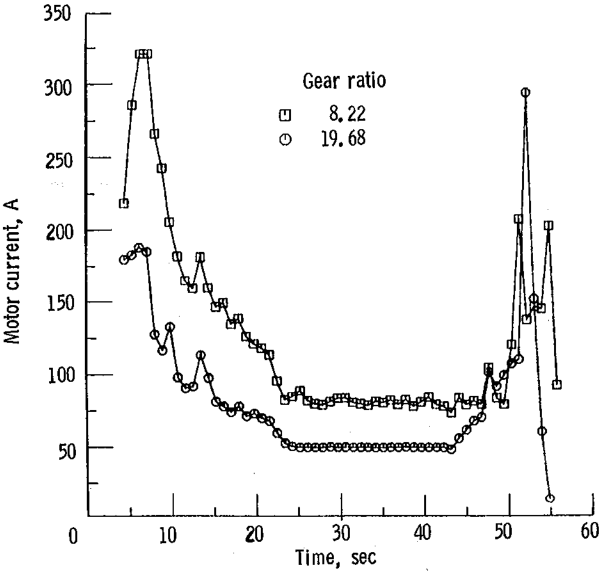

Figure 45. - Motor current as function of time for two gear ratios for SAE-J227a schedule B cycle.

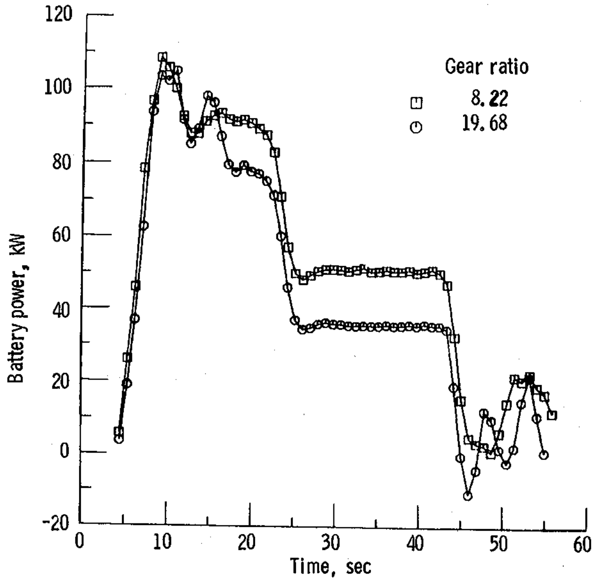

Figure 46. - Battery power as function of time for two gear ratios for SAE-J227a schedule B cycle.

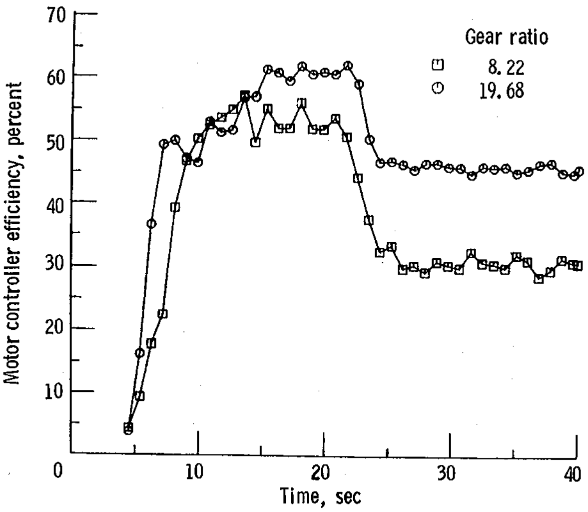

Figure 47. - Motor controller system efficiency as function of time for two gear ratios for SAE-J227a schedule B cycle.

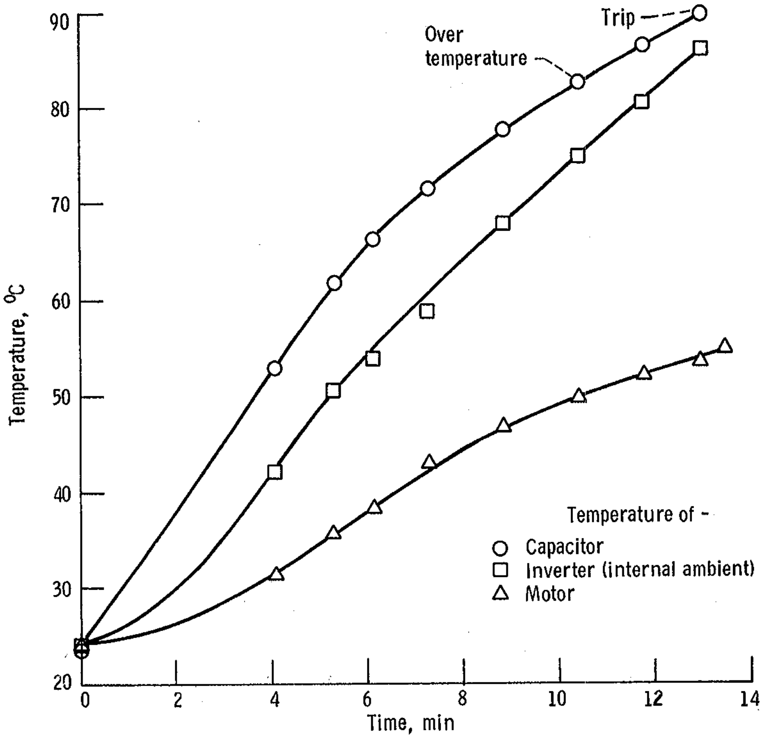

Figure 48. - Capacitor, inverter ambient, and motor temperatures as functions of time in PWM operating mode. Motor shaft power, 15 hp; motor speed, 2500 rpm.

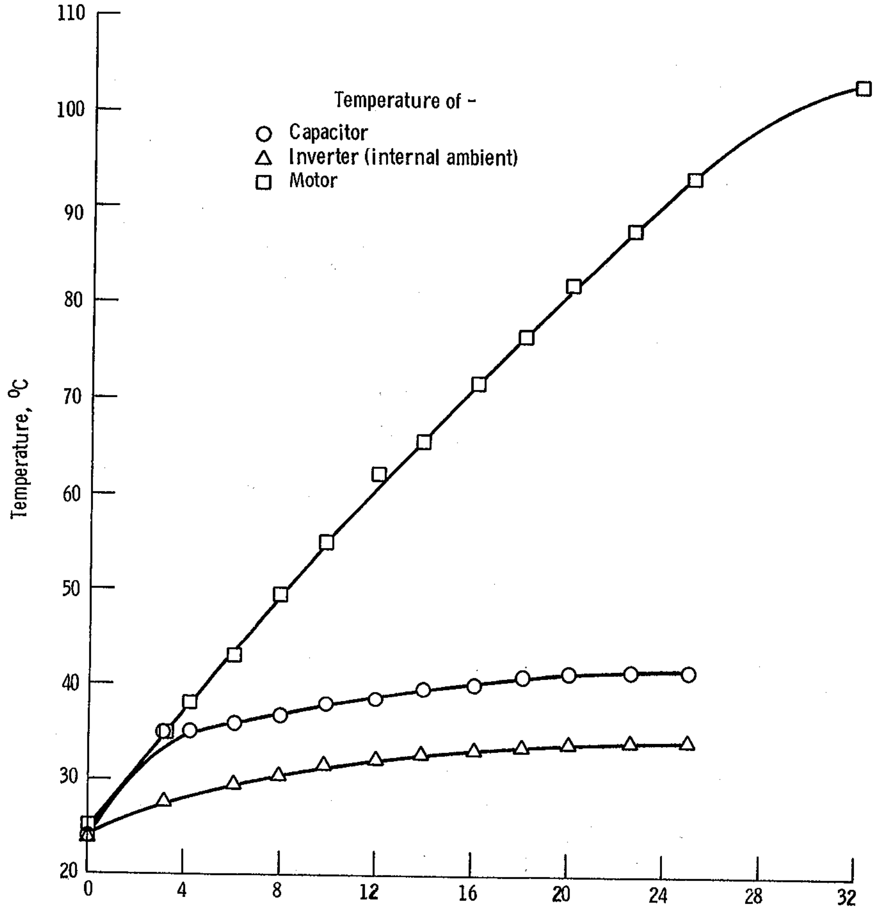

Figure 49. - Capacitor, inverter ambient, and motor temperatures as functions of time in quasi-square wave operating mode. Motor shaft power, 15 hp; motor speeds, 6000 rpm.

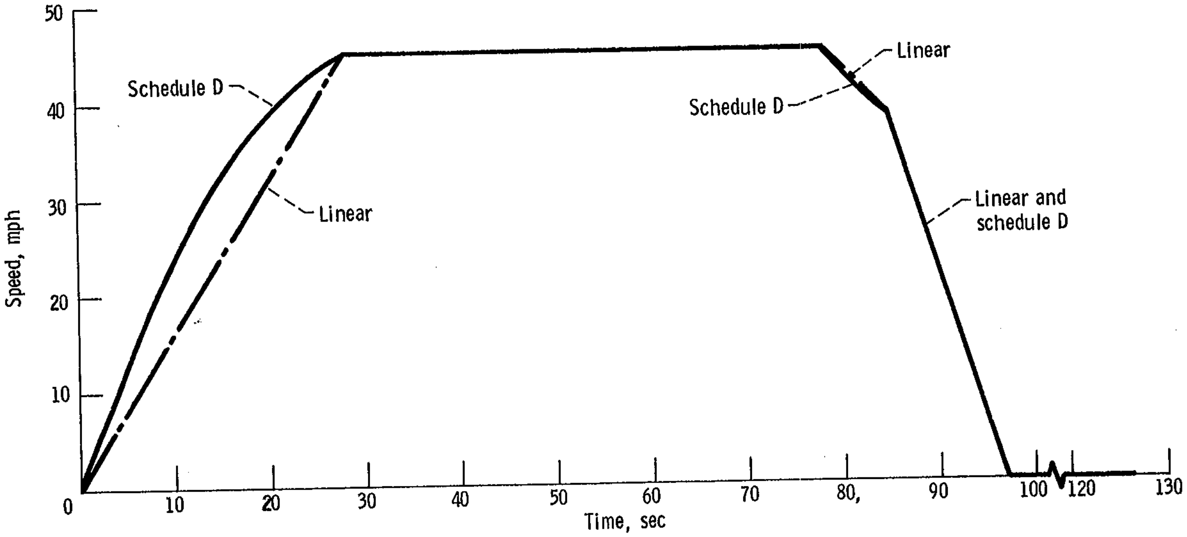

Figure 50. - Schedule D driving cycle. Acceleration, 0 to 45 mph, 28 sec; 45 mph constant, 50 sec; coast, 7 sec; brake, 12 sec; rest, 25 sec.

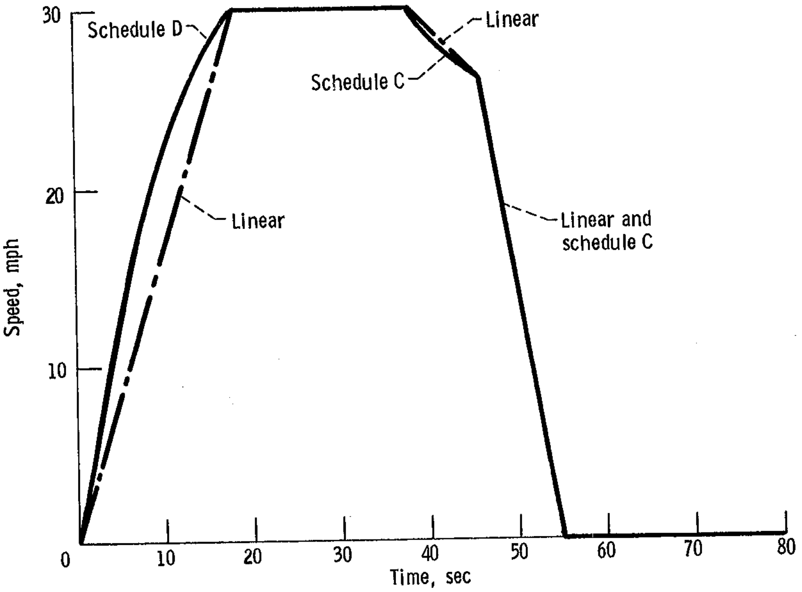

Figure 51. - Schedule C driving cycle. Acceleration, 0 to 30 mph, 18 sec; 30 mph constant, 20 sec; coast, 8 sec; brake to 0 mph, 9 sec; rest, 25 sec.

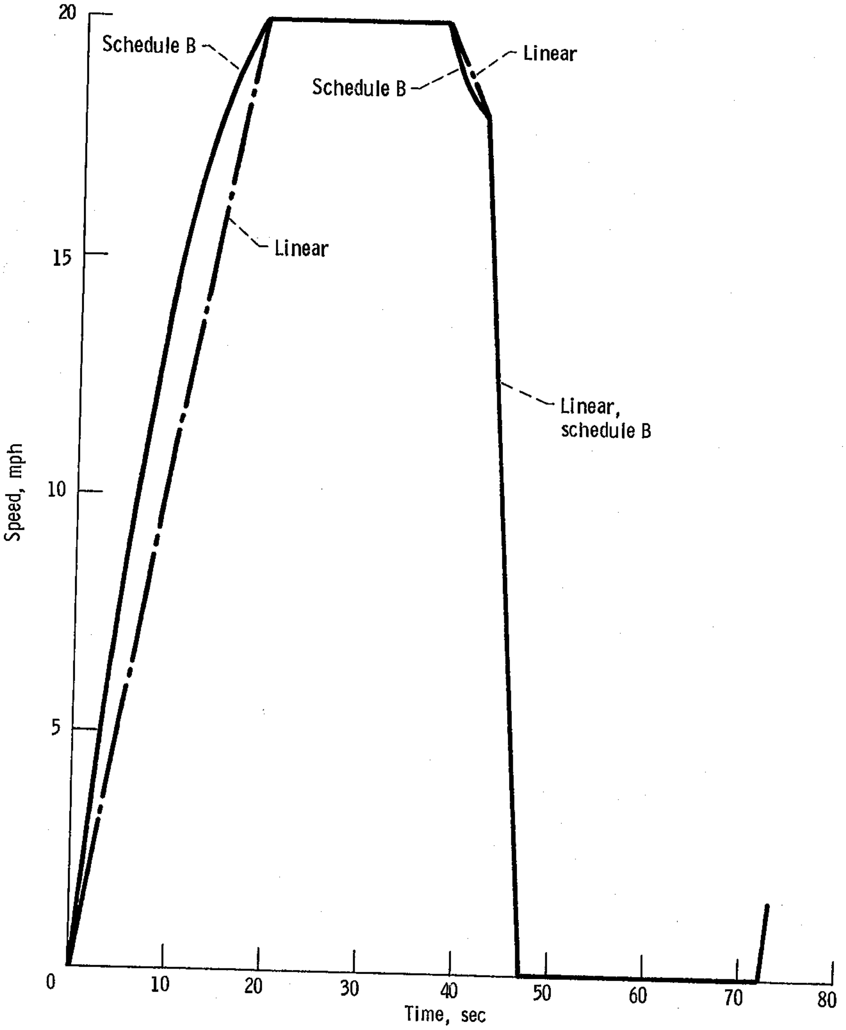

Figure 52. - Schedule B driving cycle. Acceleration, 0 to 20 mph, 19 sec; 20 mph constant, 19 sec; coast, 4 sec; brake to 0 mph, 5 sec; rest, 25 sec.

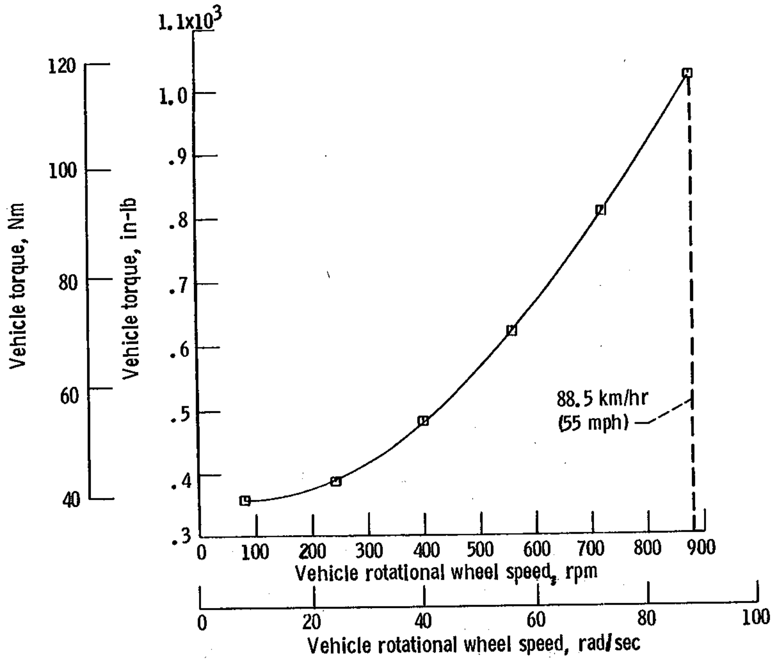

Figure 53. - Road load characteristic of vehicle torque as function of vehicle rotational wheel speed. Gear ratio, 8.22; tire radius, 0.267 m (0.875 ft); zero grade; battery terminal voltage, 120 V.

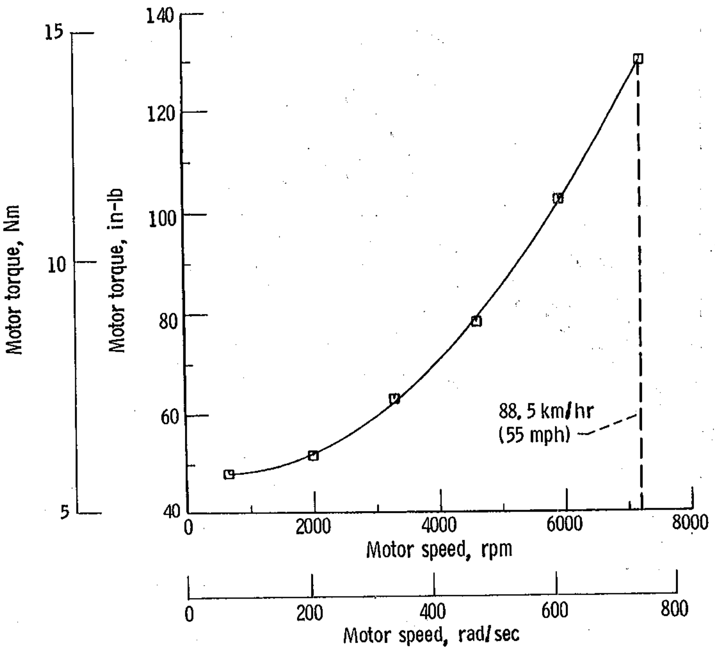

Figure 54. - Road load characteristic of motor torque as function of motor speed. Gear ratio, 8.22; tire radius, 0.267 m (0.875 ft); zero grade; battery terminal voltage, 120 V.

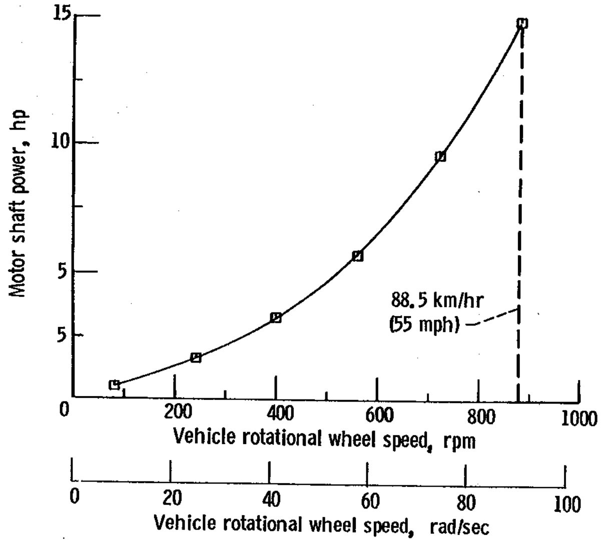

Figure 55. - Road load characteristic of motor shaft power as function of vehicle rotational wheel speed. Gear ratio, 8.22; tire radius, 0.267 m (0.875 ft); zero grade; battery terminal voltage, 120 V.

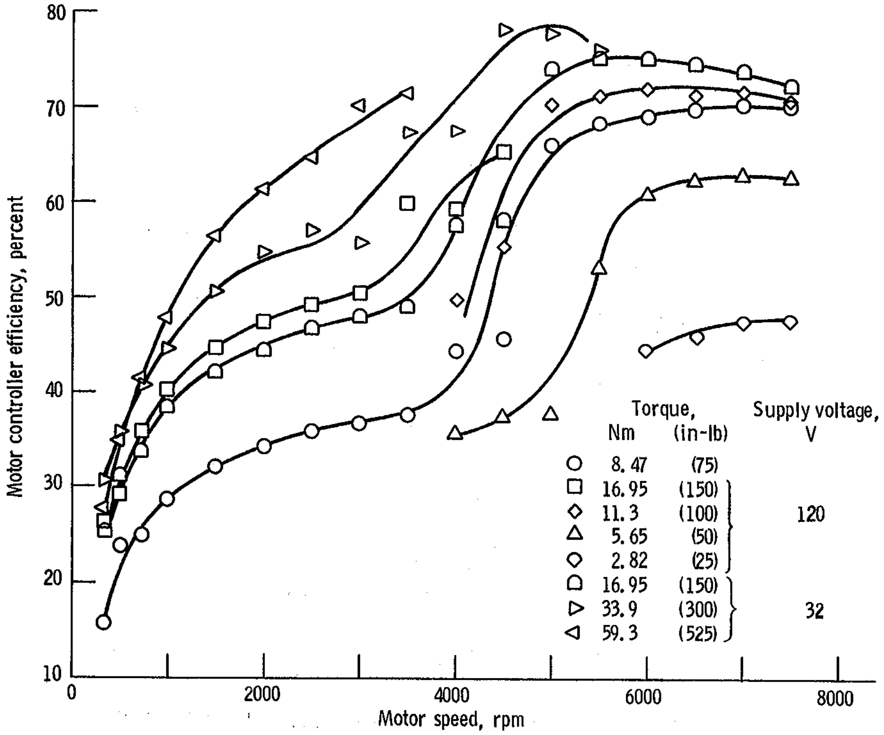

Figure 56. - Combined motor controller efficiency as function of motor speed for constant load torque. Simulator Supply.

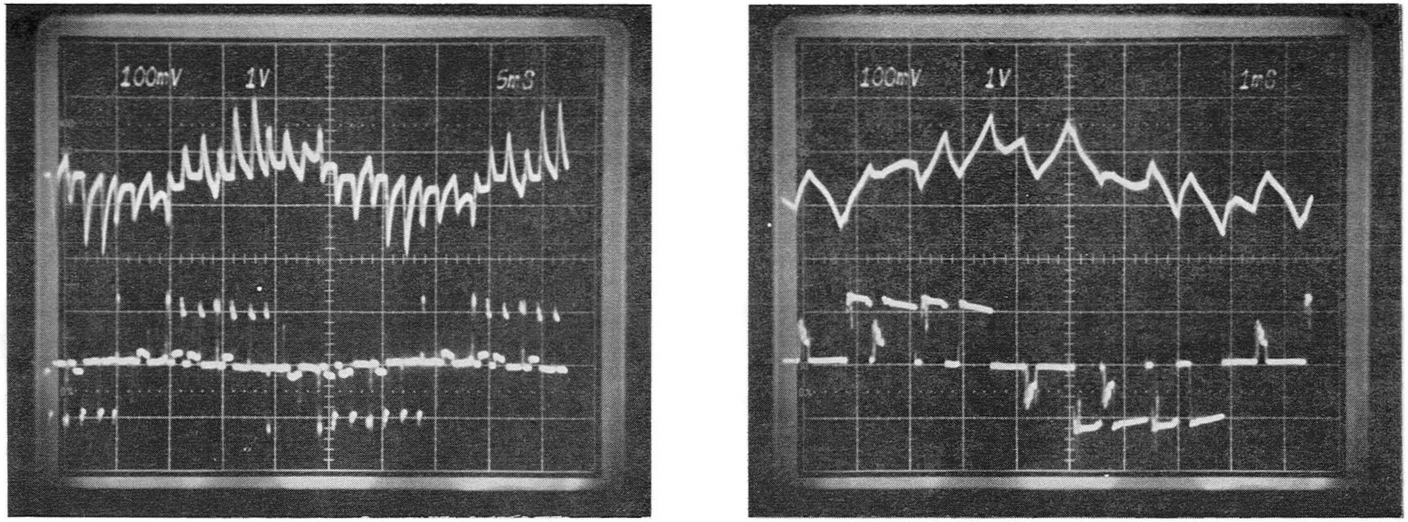

(a) Motor speed; 1060 rpm.

(b) Motor speed; 3514 rpm.

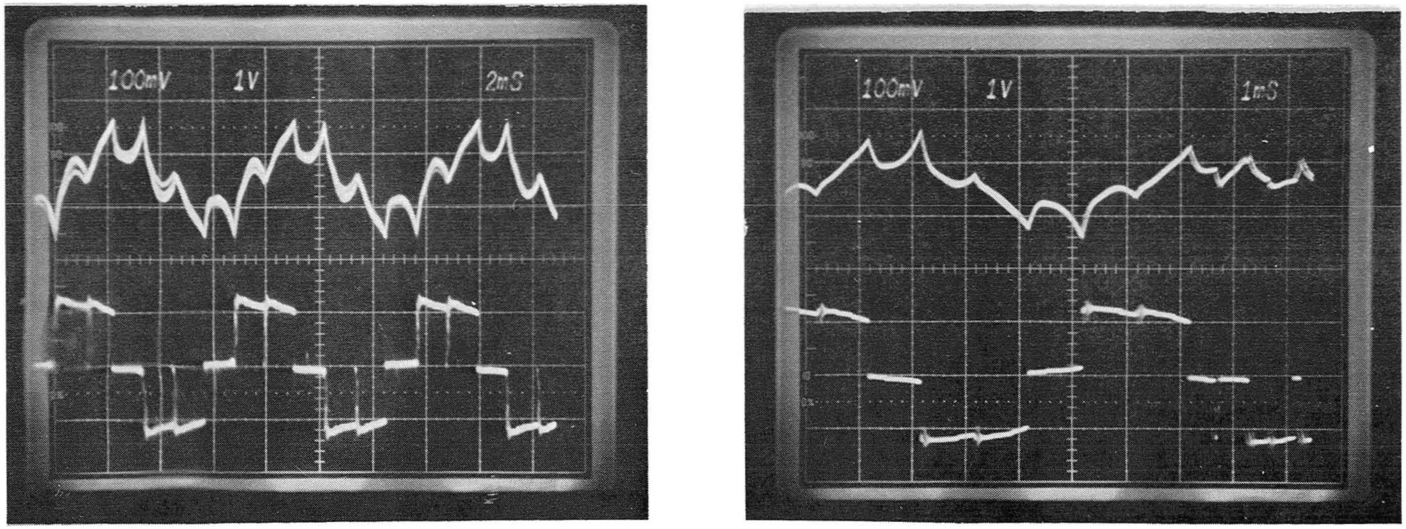

(c) Motor speed; 4316 rpm.

(d) Motor speed; 4995 rpm.

Figure 57. - Current and voltage waveforms illustrating transition from PWM to quasi-square wave operation. Upper traces denote current waveform; lower traces denote voltage waveform.

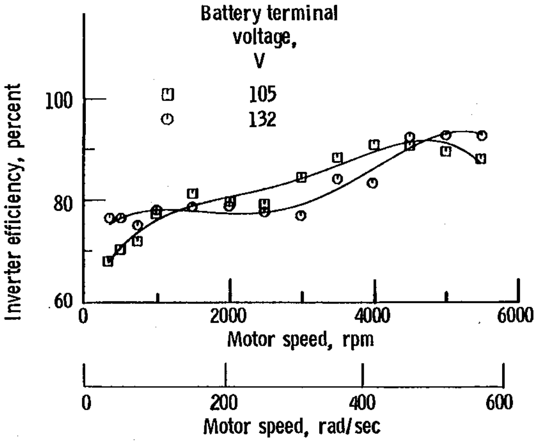

Figure 58. - Steady state characteristic of inverter efficiency as function of motor speed for constant motor torque. Motor torque, 34 Nm (300 in-lb).

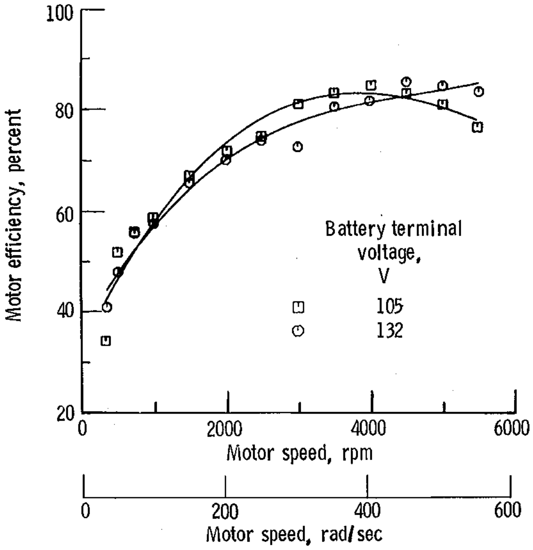

Figure 59. - Steady state characteristic of motor efficiency as function of motor speed for constant motor torque. Motor torque, 34 Nm (300 in-lb).

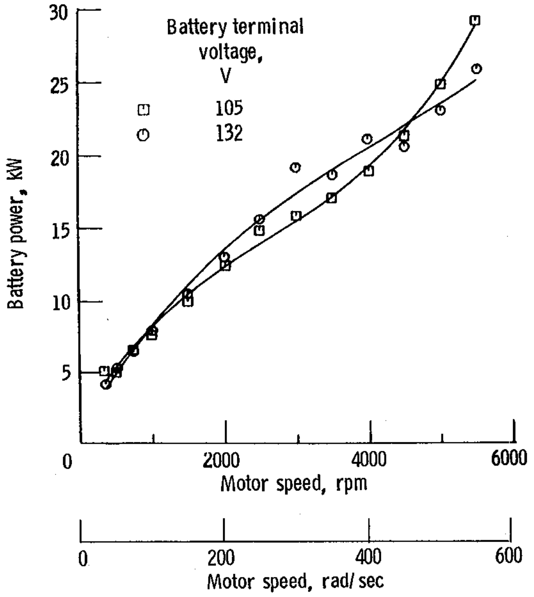

Figure 60. - Steady state characteristic of battery power as function of motor speed for constant motor torque. Motor torque, 34 Nm (300 in-lb).

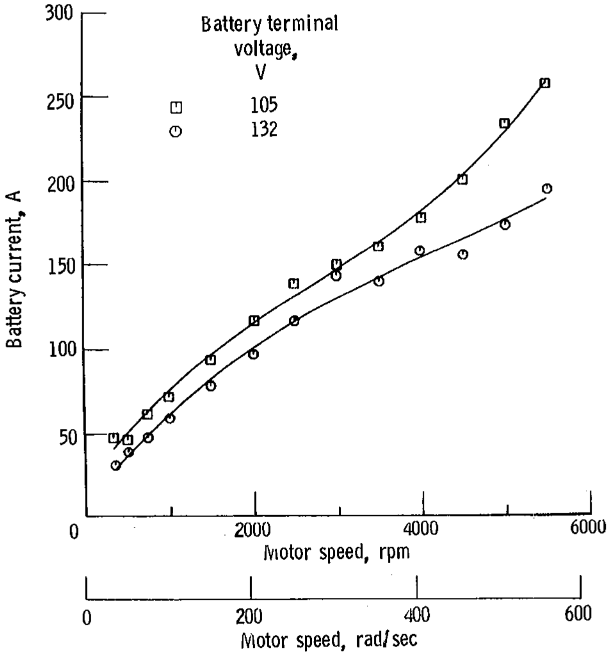

Figure 61. - Steady state characteristic of battery current as function of motor speed for constant motor torque. Motor torque, 34 Nm (300 in-lb).

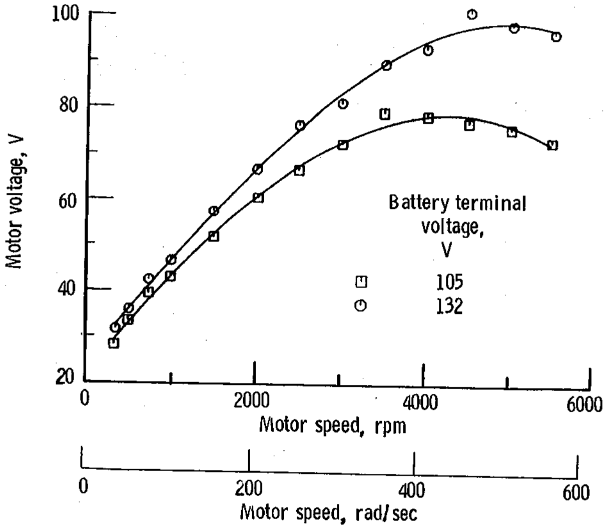

Figure 62. - Steady state characteristic of motor voltage as function of motor speed for constant motor torque. Motor torque, 34 Nm (300 in-lb).

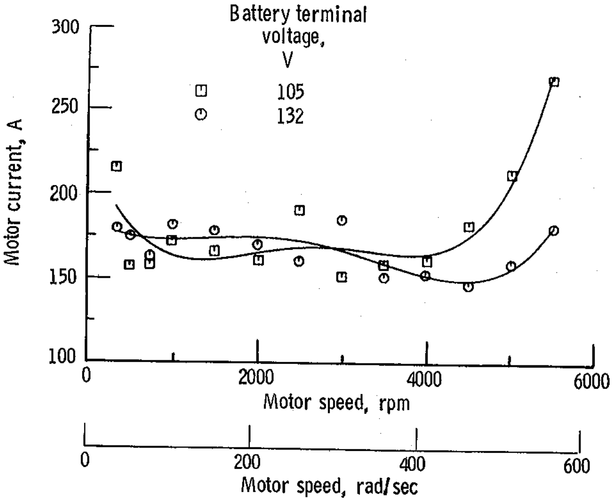

Figure 63. - Steady state characteristic of motor current as function of motor speed for constant motor torque. Motor torque, 34 Nm (300 in-lb).

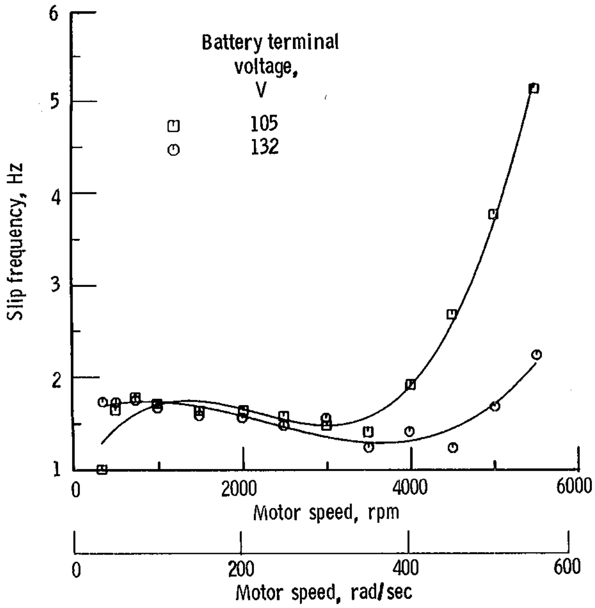

Figure 64. - Steady state characteristic of slip frequency as function of motor speed for constant motor torque. Motor torque, 34 (Nm (300 in-lb).

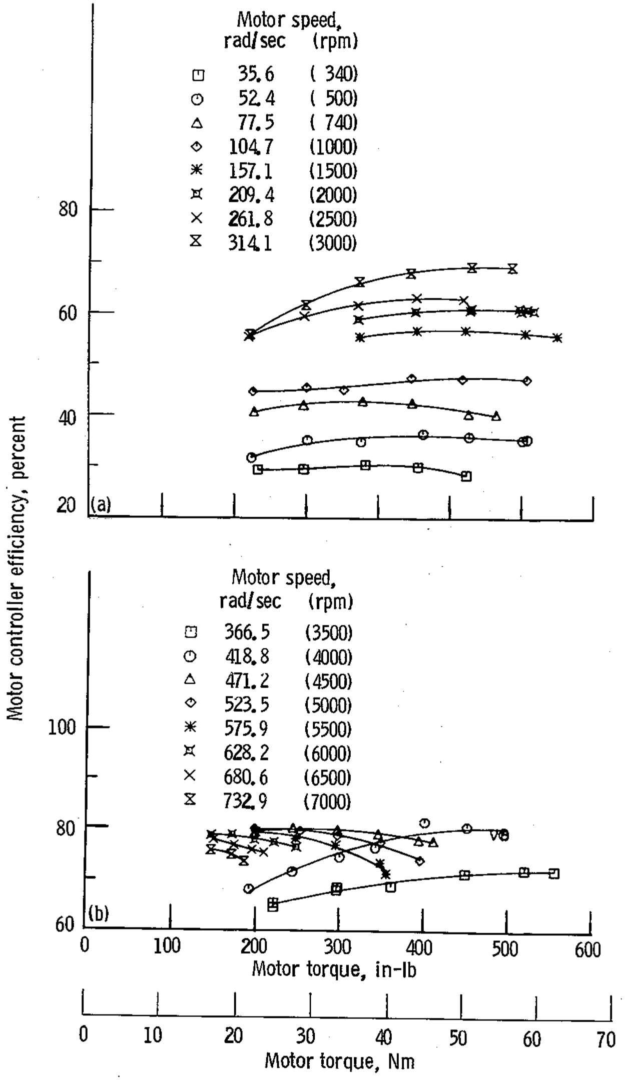

Figure 65. - Steady state characteristic of motor controller efficiency as function of motor torque for constant motor speeds. Battery terminal voltage, 120 V.

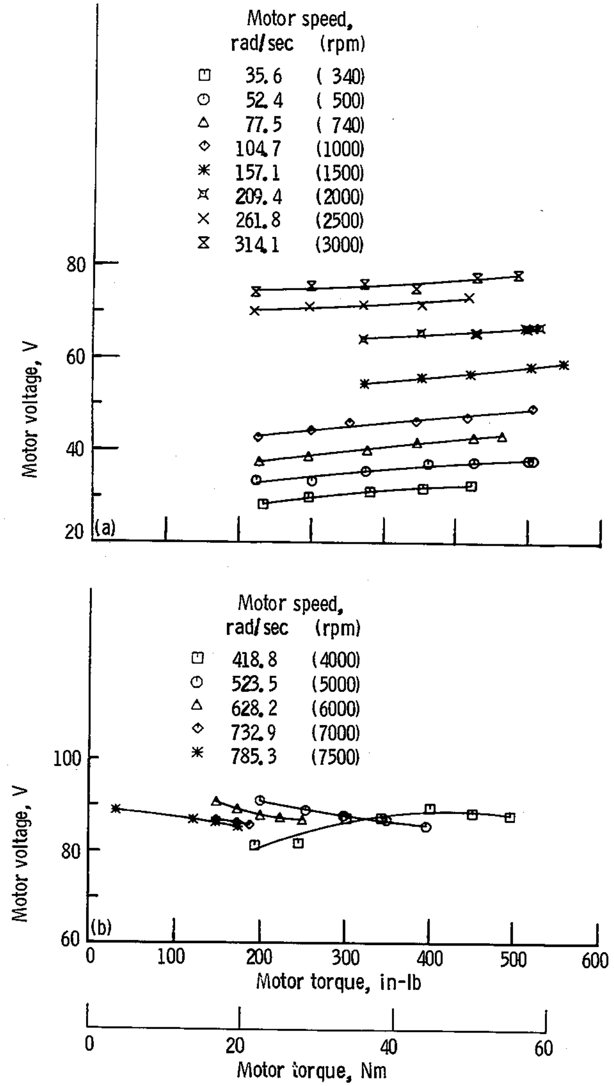

Figure 66. - Steady state characteristic of motor voltage as function of motor torque for constant motor speeds. Battery terminal voltage, 120 V.

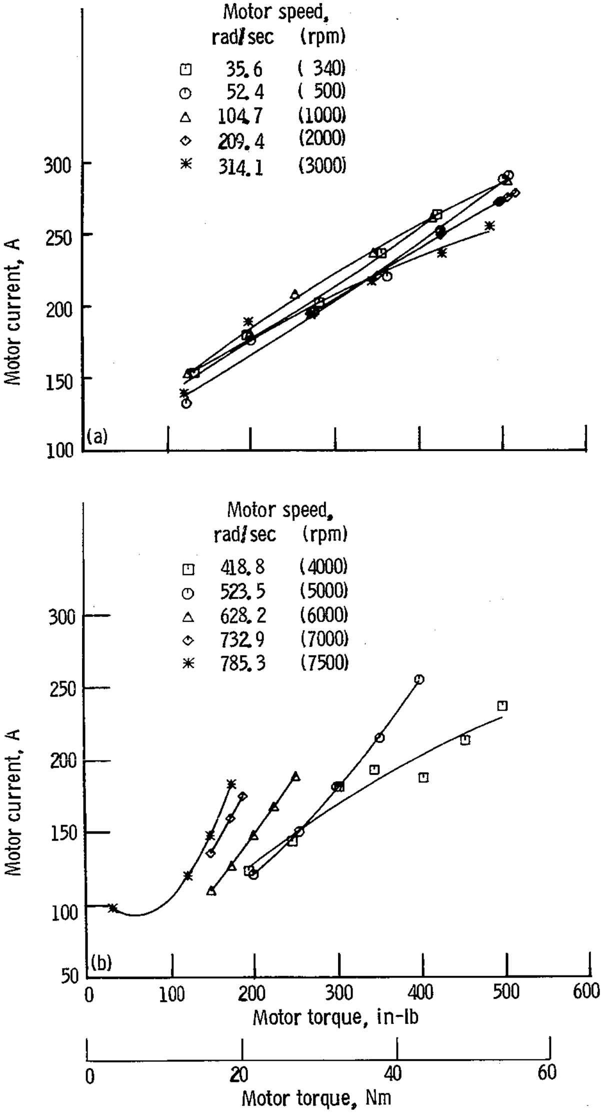

Figure 67. - Steady state characteristic of motor current as function of motor torque for constant motor speeds (SM). Battery terminal voltage, 120 V.

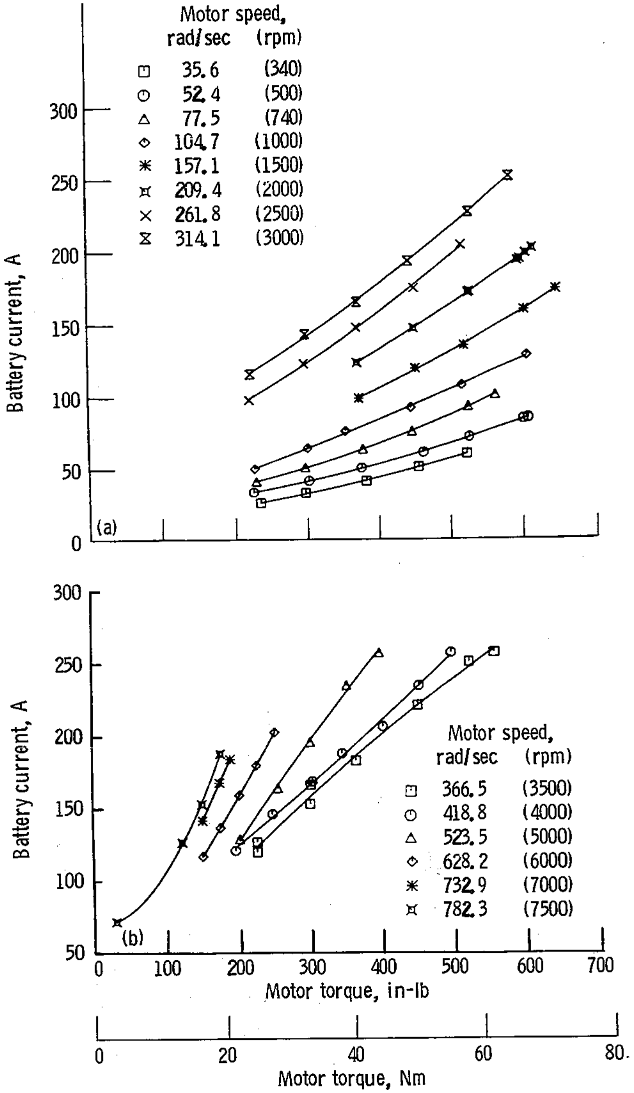

Figure 68. - Steady state characteristic of battery current as function of motor torque for constant motor speeds. Battery terminal supply, 120 V.

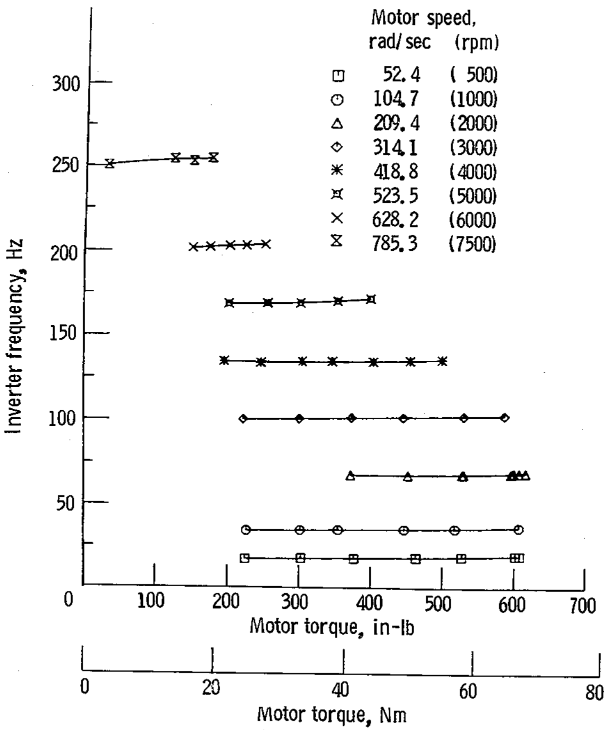

Figure 69. - Steady state characteristic of inverter frequency as function of motor torque for constant motor speeds. Battery terminal voltage, 120 V.

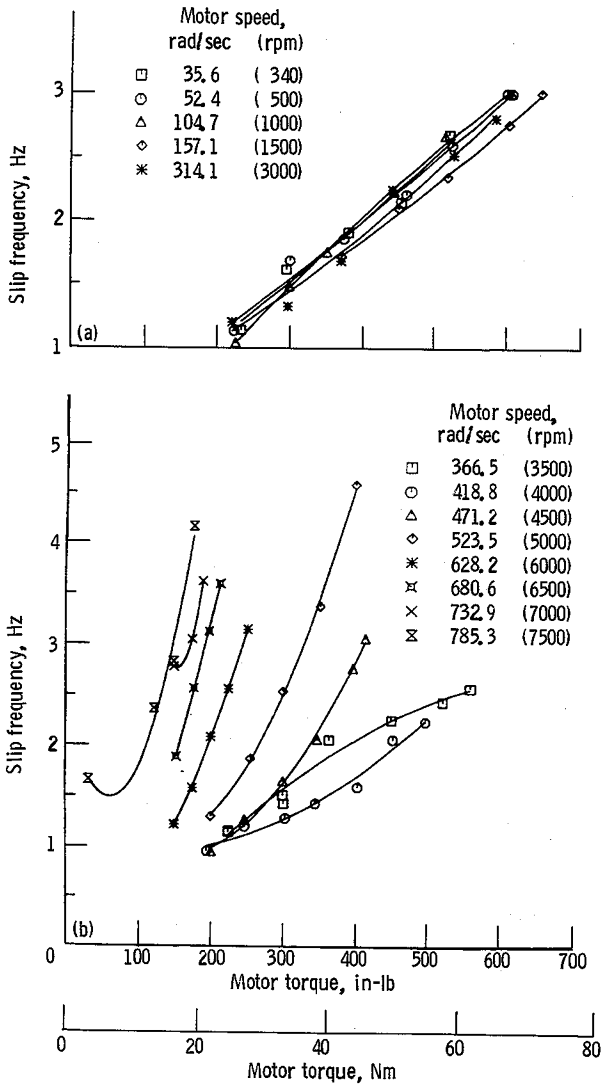

Figure 70. - Steady state characteristic of slip frequency as a function of motor torque for constant motor speeds. Battery terminal voltage, 120 V.

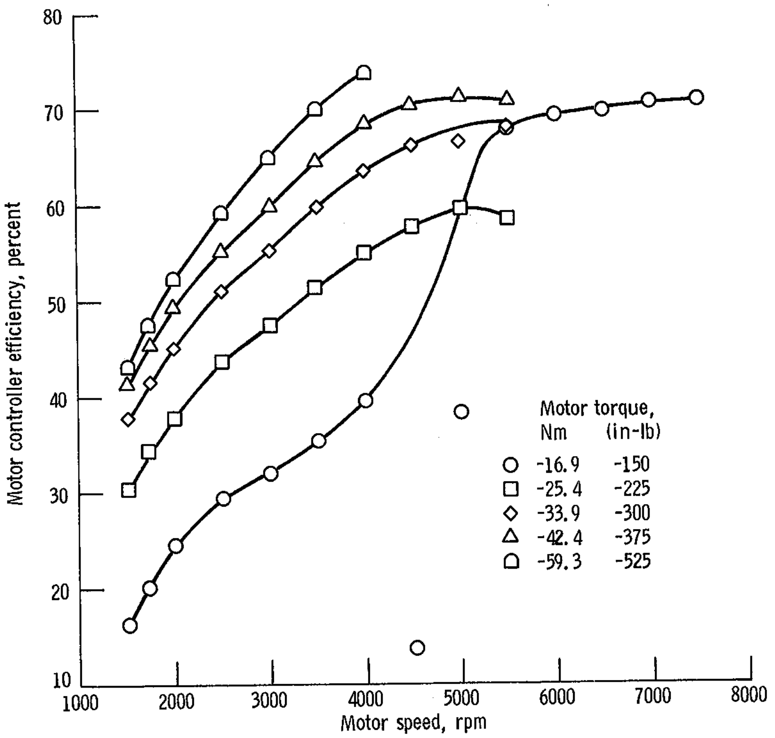

Figure 71. - Gould-Eaton system of motor controller efficiency as function of motor speed at constant negative load torques. Regeneration mode. Battery simulator supply.

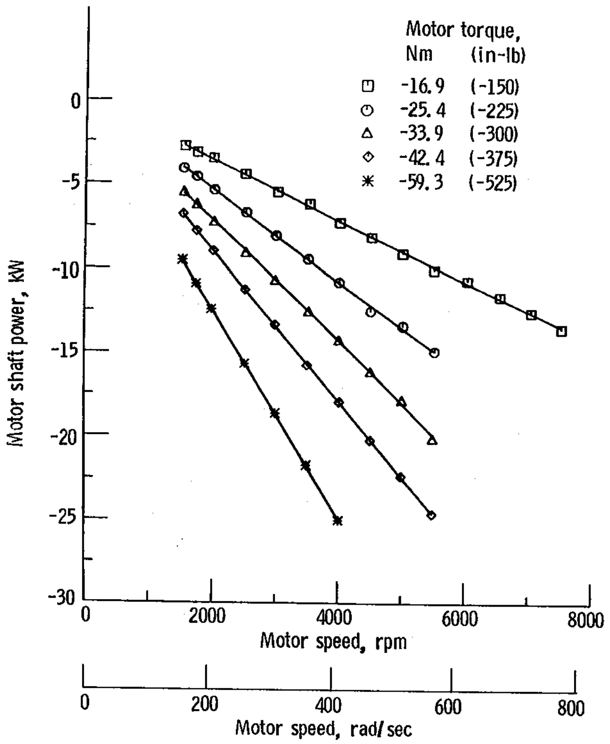

Figure 72. - Steady state characteristic of regeneration mode. Motor shaft power as function of motor speed for constant negative motor torque.

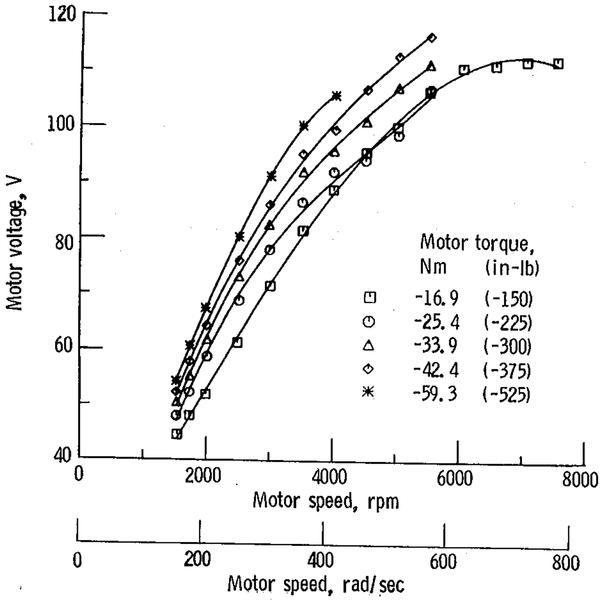

Figure 73. - Steady state characteristic of regeneration mode. Motor voltage as function of motor speed for constant negative motor torque.

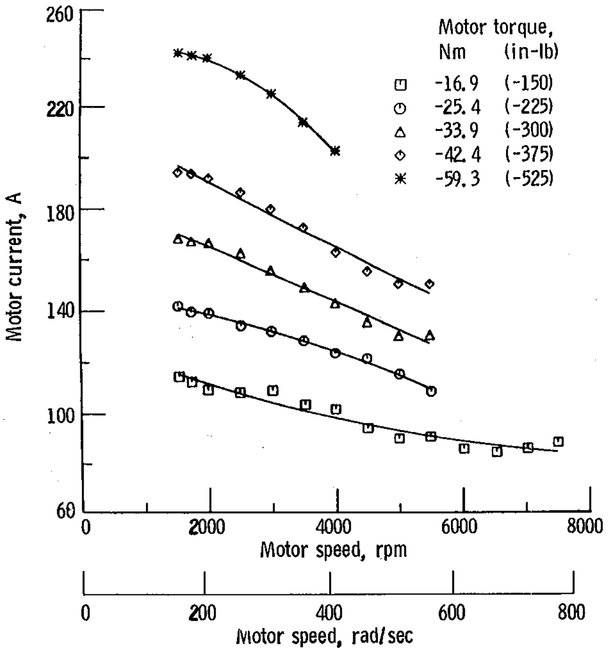

Figure 74. - Steady state characteristic of regeneration mode. Motor current as function of motor speed for constant negative motor torque.

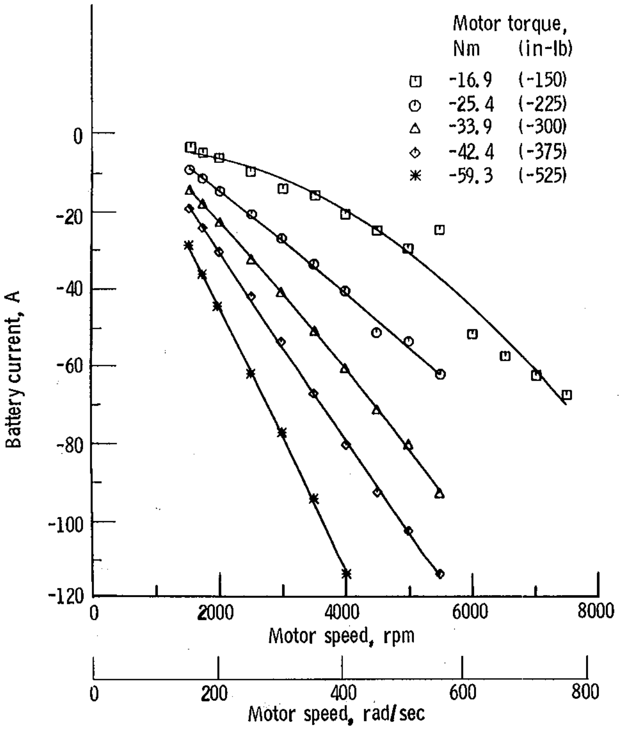

Figure 75. - Steady state characteristic of regeneration mode. Battery current as function of motor speed for constant negative motor torque.

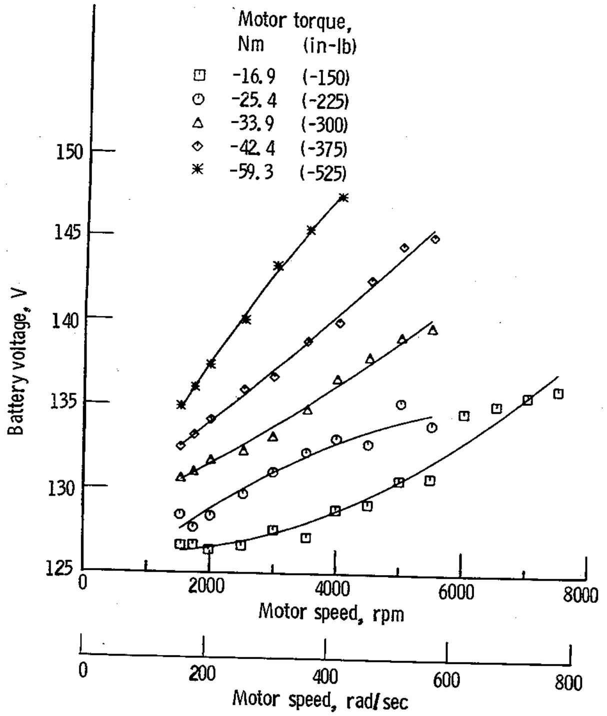

Figure 76. - Steady state characteristic of regeneration mode. Battery voltage as function of motor speed for constant negative motor torque.

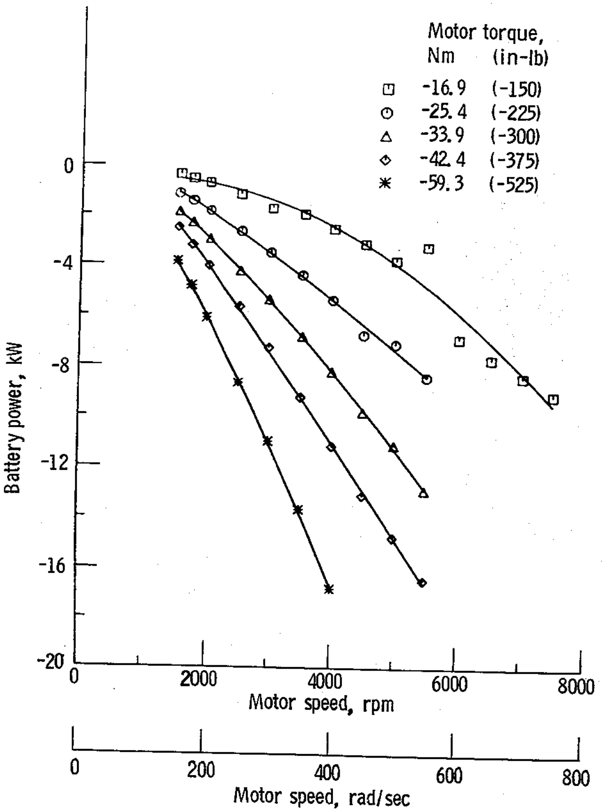

Figure 77. - Steady state characteristic of regeneration mode. Battery power as function of motor speed for constant negative motor torque.

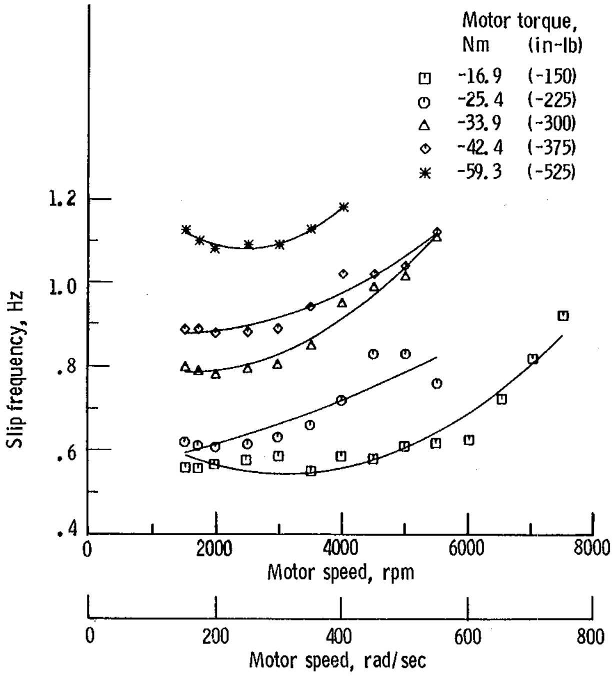

Figure 78. - Steady state characteristic of regeneration mode. Slip frequency as function of motor speed for constant negative motor torque.

1. Report No. NASA TM-83497	2. Government Accession No.	3. Recipient's Catalog No.

4. Title and Subtitle Road Load Simulator Tests of the Gould Phase I Functional Model Silicon Controlled Rectifier ac Motor Controller for Electric Vehicles	5. Report Date February 1984
	6. Performing Organization Code 778-36-06
7. Author(s) Francis Gourash	8. Performing Organization Report No. E-1831
	10. Work Unit No.
9. Performing Organization Name and Address National Aeronautics and Space Administration Lewis Research Center Cleveland, Ohio 44135	11. Contract or Grant No.
	13. Type of Report and Period Covered Technical Memorandum
12. Sponsoring Agency Name and Address U.S. Department of Energy Office of Vehicle and Engine R&D Washington, D.C. 20545	14. Sponsoring Agency ~~Code~~ Report No. DOE/NASA/51044-34

15. Supplementary Notes

Final report. Prepared under Interagency Agreement DE-AI01-77CS51044.

16. Abstract

This report presents the test results for a functional model ac motor controller for electric vehicles and a three-phase induction motor which were dynamically tested on the Lewis Research Center road load simulator. Results show that the controller has the capability to met the SAE-J227a D cycle test schedule and to accelerate a 1576-kg (3456-lb) simulated vehicle to a cruise speed of 88.5 km/hr (55 mph). Combined motor controller efficiency is 72 percent and the power inverter efficiency alone is 89 percent for the cruise region of the D cycle. Steady state test results for motoring, regeneration, and thermal data obtained by operating the simulator as a conventional dynamometer are in agreement with the contractor's previously reported data. The regeneration test results indicate that a reduction in energy requirements for urban driving cycles is attainable with regenerative braking. Test results and data in this report serve as a data base for further development of ac motor controllers and propulsion systems for electric vehicles. The controller uses state-of-the-art silicon controlled rectifier (SCR) power semiconductors and microprocessor-based logic and control circuitry. The controller was developed by Gould Laboratories under a Lewis contract for the Department of Energy's Electric and Hybrid Vehicle program.

17. Key Words (Suggested by Author(s)) SCR-ac-motor controller Electric vehicle Road load simulator Dynamic tests	18. Distribution Statement Unclassified - unlimited STAR Category 44 DOE Category UC-96

19. Security Classif. (of this report) Unclassified	20. Security Classif. (of this page) Unclassified	21. No. of pages	22. Price* A04

*For sale by the National Technical Information Service, Springfield, Virginia 22161